

NASA TECHNICAL NOTE



NASA TN D-6816

2.1

NASA TN D-6816

LOAN COPY: RETURN TO  
AFWL (DOUL)  
KIRTLAND AFB, NM



EXPERIMENTAL STATIC AERODYNAMICS  
OF A REGULAR HEXAGONAL PRISM IN  
A LOW-DENSITY HYPERVELOCITY FLOW



*by Robert W. Guy, James N. Mueller, and Louise P. Lee*  
*Langley Research Center*  
*Hampton, Va. 23365*



0133478

1. Report No. NASA TN D-6816	2. Government Accession No.	3. Recipient's Catalog No.	
4. Title and Subtitle EXPERIMENTAL STATIC AERODYNAMICS OF A REGULAR HEXAGONAL PRISM IN A LOW-DENSITY HYPERVELOCITY FLOW		5. Report Date June 1972	6. Performing Organization Code
7. Author(s) Robert W. Guy, James N. Mueller, and Louise P. Lee		8. Performing Organization Report No. L-8229	
9. Performing Organization Name and Address NASA Langley Research Center Hampton, Va. 23365		10. Work Unit No. 117-07-04-08	11. Contract or Grant No.
12. Sponsoring Agency Name and Address National Aeronautics and Space Administration Washington, D.C. 20546		13. Type of Report and Period Covered Technical Note	
15. Supplementary Notes		14. Sponsoring Agency Code	
16. Abstract <p>A regular hexagonal prism, having a fineness ratio of 1.67, has been tested in a wind tunnel to determine its static aerodynamic characteristics in a low-density hypervelocity flow. The prism tested was a 1/4-scale model of the graphite heat shield which houses the radioactive fuel for the Viking spacecraft auxiliary power supply. The basic hexagonal prism was also modified to simulate a prism on which ablation of one of the six side flats had occurred. This modified hexagonal prism was tested to determine the effects on the aerodynamic characteristics of a shape change caused by ablation during a possible side-on stable reentry.</p> <p>Aerodynamic force and moment data on the prism were obtained at an average Mach number of 12.3 and an average length Reynolds number of 1380. The experimental force data were compared with modified Newtonian theory (continuum flow regime), free molecular transfer theory (free-molecule flow regime), and a semiempirical transition "bridging" theory (transition flow regime). The force data showed the effects of flow rarefaction and were in better agreement with the estimates of the bridging theory than with either of the limiting theories. The experimental moment data from both the basic hexagonal prism and the modified hexagonal prism confirmed the stability of a side-on reentry. The moment data, as well as the smaller force data, also indicated the importance of alining the model sting with the model wake to minimize sting-interference effects on the data.</p>			
17. Key Words (Suggested by Author(s)) Low density flow Hypervelocity flow Hexagonal prism Force and moment data		18. Distribution Statement Unclassified - Unlimited	
19. Security Classif. (of this report) Unclassified	20. Security Classif. (of this page) Unclassified	21. No. of Pages 59	22. Price* \$3.00

EXPERIMENTAL STATIC AERODYNAMICS  
OF A REGULAR HEXAGONAL PRISM IN A LOW-DENSITY  
HYPERVELOCITY FLOW

By Robert W. Guy, James N. Mueller,  
and Louise P. Lee  
Langley Research Center

SUMMARY

A regular hexagonal prism, having a fineness ratio of 1.67, has been tested in a wind tunnel to determine its static aerodynamic characteristics in a low-density hypervelocity flow. The prism tested was a 1/4-scale model of the graphite heat shield which houses the radioactive fuel for the Viking spacecraft auxiliary power supply. The basic hexagonal prism was also modified to simulate a prism on which ablation of one of the six side flats had occurred. This modified hexagonal prism was tested to determine the effects on the aerodynamic characteristics of a shape change caused by ablation during a possible side-on stable reentry.

Aerodynamic force and moment data on the prism were obtained at an average Mach number of 12.3 and an average length Reynolds number of 1380. The experimental force data were compared with modified Newtonian theory (continuum flow regime), free molecular transfer theory (free-molecule flow regime), and a semiempirical transition "bridging" theory (transition flow regime). The force data showed the effects of flow rarefaction and were in better agreement with the estimates of the bridging theory than with either of the limiting theories. The experimental moment data from both the basic hexagonal prism and the modified hexagonal prism confirmed the stability of a side-on reentry. The moment data, as well as the smaller force data, also indicated the importance of aligning the model sting with the model wake to minimize sting-interference effects on the data.

INTRODUCTION

In recent years, orbital insertion and reentry of satellites and spacecraft have created the need for high-altitude high-velocity aerodynamic and heat-transfer data on bodies of various, and often aerodynamically unusual, shapes. These complex shapes make theoretical analyses difficult, especially in the transition regime between continuum and free-molecule flow.

In this paper, the low-density, hypervelocity, static aerodynamic characteristics are determined for an aerodynamically unusual shape, a regular hexagonal prism having a fineness ratio of 1.67. This shape is the same as the graphite heat shield which houses the radioactive fuel for the Viking spacecraft auxiliary power supply (radioisotopic thermoelectric generator). Safety considerations dictate that if an abort should occur, this fuel cell must survive reentry and land intact. In order to determine the probability of survival during reentry, fuel-cell orientation must be known so that the heat load to the cell can be predicted. Background information on this type of fuel cell as well as a discussion of a multiple-revolution fuel-cell reentry is contained in reference 1.

The regular hexagonal prism tested in the present investigation was a 1/4-scale model of the Viking fuel cell. It was tested at an average Mach number of 12.3, an average length Reynolds number of 1380, and a simulated altitude (based on the ratio of unit Reynolds number to Mach number) of 77.7 kilometers referenced to the length of the full-scale body (1962 U.S. Standard Atmosphere, ref. 2). The prism was tested through an angle-of-attack range of  $0^\circ$  to  $90^\circ$  (apex forward, an effective roll angle  $\psi$  of  $0^\circ$ ), an angle-of-attack range of  $0^\circ$  to  $90^\circ$  (side flat forward, an effective roll angle  $\psi$  of  $-90^\circ$ ), and a roll-angle range of  $0^\circ$  to  $-30^\circ$  (apex-to-side flat) at an angle of attack of  $90^\circ$ . The regular hexagonal prism, modified to simulate a prism with one of its six side flats ablated, was also tested through a roll-angle range of  $0^\circ$  to  $-180^\circ$  at an angle of attack of  $90^\circ$ . This modified prism was tested to determine the effects on the static aerodynamic characteristics of a possible stable side-on reentry. Similar investigations on a right circular cylinder fuel cell are reported in references 3 to 5.

The force data were compared with modified Newtonian theory (ref. 6) and free-molecule flow theory (ref. 7). In addition, the force data were compared with a semiempirical transition bridging theory (ref. 8) which was based on these limiting theories.

The present force and moment data add to the rather meager supply of experimental data on aerodynamically unusual shapes flying at high altitudes. Such data are needed for three reasons. First, they may be used to evaluate theoretical prediction methods in the transition flow regime. Second, they are necessary for the determination of vehicle orientation during reentry (for safety, reusability of vehicles, and other considerations). And, third, they are needed in the determination of the proper altitude for the removal of the protective shroud during satellite launches.

## SYMBOLS AND NOMENCLATURE

The body and wind axes systems, showing the directions of forces, moments, and angular quantities are presented in figure 1. The angles used to describe the orientation of the hexagonal prism are from reference 9. The reference area used in the force and moment coefficient equations is the product of the model length and the distance between

the side flats of the basic hexagonal prism. Reference length is the model length. The moment reference center is coincident with the longitudinal axis of the basic hexagonal prism and is located at the midpoint of the model. Measurements from this investigation are presented in the International System of Units (SI) (ref. 10).

$A_{\text{bal}}$	axial force in balance-axis system, corrected for component interaction
$A'_{\text{bal}}$	axial force in balance-axis system, uncorrected for component interaction
$A$	reference area, (Ld)
$B$	constant in equation (7)
$C_A$	axial-force coefficient in body-axis system (along $X_B$ ), $\frac{F_A}{q_\infty A}$
$C_C$	crosswind-force coefficient in wind-axis system (along $Y_w$ ), $\frac{F_C}{q_\infty A}$
$C_D$	drag-force coefficient in wind-axis system (along $X_w$ ), $\frac{F_D}{q_\infty A}$
$C_{\text{FM}}$	arbitrary aerodynamic coefficient as predicted by free-molecule flow theory (eq. (12))
$C_L$	lift-force coefficient in wind-axis system (along $Z_w$ ), $\frac{F_L}{q_\infty A}$
$C_l$	rolling-moment coefficient in body-axis system (about $X_B$ ), $\frac{M_{X,B}}{q_\infty AL}$
$C_{\text{MN}}$	arbitrary aerodynamic coefficient as predicted by modified Newtonian theory (eq. (12))
$C_m$	pitching-moment coefficient in body-axis system (about $Y_B$ ), $\frac{M_{Y,B}}{q_\infty AL}$
$C_N$	normal-force coefficient in body-axis system (along $Z_B$ ), $\frac{F_N}{q_\infty A}$
$C_n$	yawing-moment coefficient in body-axis system (about $Z_B$ ), $\frac{M_{Z,B}}{q_\infty AL}$
$C_{\text{TR}}$	arbitrary aerodynamic coefficient as predicted by the bridging theory for transition regime (eq. (12))

$C_Y$	side-force coefficient in body-axis system (along $Y_B$ ), $\frac{F_Y}{q_\infty A}$
$d$	distance between side flats of basic hexagonal prism
$F_A$	axial force in body-axis system (along $X_B$ )
$F_C$	crosswind force in wind-axis system (along $Y_w$ )
$F_D$	drag force in wind-axis system (along $X_w$ )
$F_L$	lift force in wind-axis system (along $Z_w$ )
$F_N$	normal force in body-axis system (along $Z_B$ )
$F_Y$	side force in body-axis system (along $Y_B$ )
$f_n$	normal accommodation coefficient (eq. (10))
$f_t$	tangential accommodation coefficient (eq. (11))
$H$	enthalpy
$K$	constant in modified Newtonian theory (eq. (9))
$L$	reference length (length of model)
$M$	Mach number
$M_{X,B}$	rolling moment in body-axis system (about $X_B$ )
$M_{Y,B}$	pitching moment in body-axis system (about $Y_B$ )
$M_{Z,B}$	yawing moment in body-axis system (about $Z_B$ )
$N_{bal}$	normal force in balance-axis system, corrected for component interaction
$N'_{bal}$	normal force in balance-axis system, uncorrected for component interaction
$N_{Re}$	unit Reynolds number, $\frac{\rho V}{\mu}$

$N_{Re,L}$	Reynolds number, $\frac{\rho V L}{\mu}$
$p$	pressure
$q$	dynamic pressure, $\frac{\rho V^2}{2}$
$S$	molecular speed ratio, $\sqrt{\frac{\gamma}{2}} M$
$T$	temperature
$V$	velocity
$\bar{v}_L$	hypersonic viscous parameter, $\frac{M}{\sqrt{N_{Re,L}}}$
$X_B, Y_B, Z_B$	body-fixed axes; origin at center of gravity; $X_B$ coincident with a longitudinal axis of the body (fig. 1)
$X_w, Y_w, Z_w$	wind axes; origin at center of gravity; $X_w$ aligned with relative wind; $Y_w, Z_w$ nonrolling about the $X_w$ axis (fig. 1)
$\gamma$	ratio of specific heats
$\epsilon$	angle of sting balance relative to wind direction
$\eta$	angle between tangent to body surface and wind direction
$\theta$	sting offset angle
$\lambda$	mean free path length
$\mu$	dynamic viscosity
$\rho$	mass density
$\sigma$	resultant angle of attack defined by $X_B$ axis and velocity vector (fig. 1)
$\psi$	effective roll angle; angular inclination of the $Z_B$ axis from the projection of the velocity vector in the $Y_B, Z_B$ plane

Subscripts:

- b            model wall
- L            based on reference length
- t,1          plenum chamber stagnation condition
- t,2          stagnation condition behind a normal shock
- $\infty$         free-stream conditions

APPARATUS AND TESTS

Tunnel and Test Conditions

The tunnel used in this investigation was the 0.305-meter hypersonic arc tunnel at the Langley Research Center (fig. 2) with air as the test gas. A magnetically rotated arc heats the air and a 5° half-angle nozzle expands it from the 0.55-cm-diameter throat to the 0.305-meter test section. A five-stage steam ejector provides sufficient vacuum for continuous tunnel operation.

Tunnel flow properties were determined from measurements and from calculations. Measured properties were stagnation chamber pressure, pitot pressure, tunnel mass flow rate, and total enthalpy (determined as a function of stagnation chamber pressure, tunnel mass flow rate, and effective sonic-throat area from previous calorimeter measurements (ref. 11)). Free-stream properties were calculated by using the Cornell chemical non-equilibrium gas expansion computer program (ref. 12) which had been modified to account approximately for vibrational nonequilibrium (ref. 11). The nonequilibrium stream properties were functions of stagnation chamber pressure and temperature, throat size and nozzle geometry, and measured pitot pressure.

Average test conditions for the present investigation are given in the following table. Specific test conditions for individual tests are presented in table I.

Test parameter	Average value	Test parameter	Average value
$P_{t,1}$ , N/m <sup>2</sup> . . . . .	$8.36 \times 10^5$	$V_{\infty}$ , m/s . . . . .	3325
$H_{t,1}$ , MJ/kg . . . . .	7.71	$q_{\infty}$ , N/m <sup>2</sup> . . . . .	587
$T_{t,1}$ , K . . . . .	4440	$P_{t,2}$ , N/m <sup>2</sup> . . . . .	1076
$M_{\infty}$ . . . . .	12.3	$N_{Re,\infty,L}$ . . . . .	1380
$p_{\infty}$ , N/m <sup>2</sup> . . . . .	5.43	$\bar{v}_{\infty,L}$ . . . . .	0.331
$\rho_{\infty}$ , kg/m <sup>3</sup> . . . . .	$1.07 \times 10^{-4}$	$\lambda_{\infty}$ , cm . . . . .	0.058
$T_{\infty}$ , K . . . . .	162		

In order to assess property gradients, longitudinal and lateral pitot pressure surveys were taken near the test-section area occupied by the hexagonal prism model. The longitudinal surveys showed that the dynamic pressure varied about  $2\frac{1}{2}$  percent over a distance equivalent to the model length. Lateral pitot pressure surveys, in the presence of and approximately 12.7 cm upstream of the model, indicated no variation in dynamic pressure over a distance equal to the projected length of the model when the sting balance was aligned with the flow. With the sting balance at the maximum angle to the flow ( $\epsilon \approx 16^\circ$ ), the lateral surveys indicated an average variation of  $2\frac{1}{2}$  percent in dynamic pressure in a distance equivalent to one model length.

The effects of conical flow (ref. 13) on the force and moment data were assessed analytically by assuming maximum flow angularity over the model (total subtended angle of  $1.25^\circ$ ). The effects on the forces were found to be small compared with the standard deviation of the experimental data. (See "Error Analysis" and table II). However, the calculated conical-flow effects on the moments were of the order of the standard deviation. Conical-flow effects should be minimized somewhat, however, by the viscous contouring of the thick boundary layer in the low-density high Mach number nozzle. (See ref. 14.)

### Models

The 1/4-scale basic hexagonal prism and the modified hexagonal prism (modified to simulate ablation of one of the six side flats) are presented, with dimensions, in figure 3. The modified prism was designed to represent a fuel cell that might reenter in a side-on stable condition rather than in a spinning or a tumbling mode. Both prisms were machined from an aluminum alloy to minimize weight (50 g) and to reduce model temperature gradients during the tests.

Several models with balance wells drilled at different sting offset angles  $\theta$  were required to cover the desired angle of attack and roll-angle ranges because the tunnel's circular-arc sector (used to vary angle of attack) was limited to a total travel of  $25^\circ$  ( $\epsilon = -16^\circ$  to  $9^\circ$ ). Some of these models are shown in the photograph in figure 4(a). A hexagonal prism model is shown mounted on the sting balance with the sting attached to the circular-arc sector of the tunnel in the photograph in figure 4(b). In order to illustrate the angle-of-attack range attainable with a particular model, a model with a sting offset angle of  $45^\circ$  is shown attached to the sting in the drawing in figure 5(a). By rotating the model-balance system  $180^\circ$ , this same model was used to obtain other angles of attack. (See fig. 5(b).)

### Instrumentation

Two strain-gage force balances were used in the test series. The first was a three-component, uncooled balance with design limits for a normal load of 0.22 N, an axial load

of 2.2 N, and a pitching moment of 1.69 cm-N. It was used to measure only normal and axial loads and the balance moment center was located near the base of the model. (Moments were recorded for use in correcting for component interaction during data reduction.) The second was a two-component, uncooled balance with design limits for a normal force of 0.44 N and a pitching moment of 0.56 cm-N. It was used to measure only the moments, and the balance moment center was located at the center of gravity of the model. (Normal force was recorded for use in correcting for component interaction.)

Pitot pressures (for use in determining free-stream properties) were obtained by using a 0.475-cm-diameter flat-faced water-cooled cylindrical probe. They required neither a viscous correction (refs. 15 and 16) nor an orifice correction (ref. 17). The pressures were measured with a capacitance transducer.

The sting-balance angle relative to the stream  $\epsilon$  was measured electrically by the resistance change of a precalibrated precision potentiometer. This measurement, along with the others previously mentioned, was recorded on a 52-channel dry-develop oscillograph.

#### Test Procedure

The model, balance, and circular-arc sector were oriented so that the model weight acted in a plane perpendicular to the plane in which the forces and moments were measured. Since the models were mounted on the center of rotation of the circular-arc sector, they stayed in essentially the same location in the test section when the resultant angles of attack  $\sigma$  or effective roll angles  $\psi$  were varied.

Preliminary tests, with the uncooled model and balance stationary, indicated that the measured forces and moments were unaffected by model temperature for test durations less than 12 seconds. With this time constraint, the test procedure for obtaining the longitudinal ( $\psi = 0^\circ$ ;  $\sigma = 0^\circ$  to  $90^\circ$ ), lateral ( $-\psi = 90^\circ$ ;  $\sigma = 0^\circ$  to  $90^\circ$ ), and roll data ( $\sigma = 90^\circ$ ;  $-\psi = 0^\circ$  to  $180^\circ$ ) was as follows (see fig. 5):

(1) The model was mounted on the balance support system with the sting balance aligned with the flow. It was left in this position for 5 seconds after the tunnel was started to allow the flow to become established.

(2) Then, the model was rotated ( $12^\circ/\text{sec}$ ) to its angular limit in one direction. (Travel was stopped by a limit switch triggered by a tab on the circular-arc sector.) It was held in this position for about 1 second.

(3) Next, the model was rotated to its angular limit in the opposite direction and held in this position for 1 second.

(4) Finally, with the model in this position, the pitot probe was inserted into the flow and pitot pressure was measured near the model tip on the tunnel center line. After allow-

ing the required 2 seconds for the pressure measurement to reach a steady-state level, the tunnel flow was stopped.

On the next test, the model and the sting balance were rotated 180°. This rotation provided a duplicate zero-sting-alinement data point (to check stream angularity) and two new data points.

## DATA REDUCTION

The strain-gage data were measured from the oscillograph tapes and reduced to forces and moments by use of the balance sensitivity and calibration constants. The force data at this point were  $N'_{bal}$  and  $A'_{bal}$ , that is, the forces normal and parallel to the balance axis. Moment data were acquired without the necessity of transferring the moments since the balance moment center was located at the model center of gravity on the moment tests. The data were then corrected for balance component interaction. Finally, the corrected balance force data,  $N_{bal}$  and  $A_{bal}$ , were reduced to forces in the body- and wind-axis systems by the following equations (see fig. 6):

Wind-axis system:

$$\left. \begin{array}{l} F_L(\text{longitudinal}) \\ F_C(\text{lateral}) \\ F_C(\text{roll}) \end{array} \right\} = N_{bal} \cos \epsilon - A_{bal} \sin \epsilon \quad (-90^\circ \leq \epsilon \leq 90^\circ) \quad (1)$$

$$\left. \begin{array}{l} F_D(\text{longitudinal}) \\ F_D(\text{lateral}) \\ F_D(\text{roll}) \end{array} \right\} = N_{bal} \sin \epsilon + A_{bal} \cos \epsilon \quad (-90^\circ \leq \epsilon \leq 90^\circ) \quad (2)$$

Body-axis system:

$$\left. \begin{array}{l} F_N(\text{longitudinal}) \\ F_Y(\text{lateral}) \\ F_Y(\text{roll}) \end{array} \right\} = N_{bal} \cos \theta + A_{bal} \sin \theta \quad (0^\circ \leq \theta \leq 90^\circ) \quad (3)$$

$$\left. \begin{array}{l} F_A(\text{longitudinal}) \\ F_A(\text{lateral}) \\ F_N(\text{roll}) \end{array} \right\} = -N_{bal} \sin \theta + A_{bal} \cos \theta \quad (0^\circ \leq \theta \leq 90^\circ) \quad (4)$$

$$\left. \begin{array}{l} F_N(\text{longitudinal}) \\ F_Y(\text{lateral}) \\ F_Y(\text{roll}) \end{array} \right\} = -N_{\text{bal}} \sin(\theta - 90^\circ) + A_{\text{bal}} \cos(\theta - 90^\circ) \quad (90^\circ \leq \theta \leq 180^\circ) \quad (5)$$

$$\left. \begin{array}{l} F_A(\text{longitudinal}) \\ F_A(\text{lateral}) \\ F_N(\text{roll}) \end{array} \right\} = -N_{\text{bal}} \cos(\theta - 90^\circ) - A_{\text{bal}} \sin(\theta - 90^\circ) \quad (90^\circ \leq \theta \leq 180^\circ) \quad (6)$$

Free-stream dynamic pressure was obtained from measured pitot pressure, which, in hypersonic flow, may be closely approximated by the product  $\rho_\infty V_\infty^2$  (ref. 16), that is,

$$p_{t,2} = B\rho_\infty V_\infty^2 \quad (7)$$

The factor  $B$  is weakly dependent on the ratio of specific heats of the gas. For these tests,  $B$  was taken to be 0.925 for the known nonequilibrium flow conditions (ref. 11). Rearrangement of equation (7) gives the free-stream dynamic pressure for the present tests as

$$q = \frac{1}{2} \rho_\infty V_\infty^2 = 0.54p_{t,2} \quad (8)$$

The reference area used in the force and moment coefficient equations was the product of model length and the distance between the side flats of the basic hexagonal prism. Reference length was model length. (See fig. 3.)

## ERROR ANALYSIS

### Systematic Errors

The force and moment coefficients correspond to the total measured forces and moments on the model and thus include the effects of the pressure in the balance cavity; that is, no corrections to the data have been made to account for the presence of the sting. The moment coefficients and the smaller force coefficients show effects of sting interference. In reference 18, sting-support interference was investigated for a blunt model-support system similar to that of the present study. The interference was especially noticeable on pitching-moment data, the worse effects occurring at the lower Reynolds numbers. To minimize this effect, the suggestion was made in reference 18 that the sting support should be aligned closely with the free wake behind the model. With this in mind, heaviest emphasis in this paper is placed on data taken with the sting balance aligned with the free-stream flow direction.

## Random Errors

A random-error analysis of some of the experimental force and moment data was performed according to the method presented in reference 19. The analysis included only data points taken with the sting balance aligned with the free-stream flow direction. This analysis gave an indication of the random errors over the entire angle range considered. Both the maximum uncertainty and the standard deviation were calculated for the points mentioned. (The results are presented in table II.) The standard deviations are shown as error bars on the shaded symbols in the figures if the error limits exceeded the symbol size. The analysis included possible errors in reading the oscillograph tapes, balance calibrations, pressure transducer output, angular location of the model, and model reference dimensions.

## THEORY

The experimental aerodynamic force data were compared with modified Newtonian flow theory (ref. 6), free-molecule flow theory (ref. 7), and a semiempirical transition bridging theory (ref. 8). The moment data were not compared with these theories since each theory predicts zero moments about the model center of gravity.

The modified Newtonian and free-molecule flow theories were applied to the hexagonal prism to predict the pressures and shear stresses acting on the various surfaces of the model. The pressure on a surface from modified Newtonian theory is (ref. 6):

$$p = p_{\infty} + Kq_{\infty} \sin^2 \eta \quad (9)$$

where  $\eta$  is the angle between the body surface and the free-stream velocity vector and  $K = 2B = 1.85$  in the present study. Surface shear stress is zero in the Newtonian approximation. The pressure on a surface from free-molecule flow theory is (ref. 7):

$$p = \frac{\rho_{\infty} V_{\infty}^2}{2S_{\infty}^2} \left\{ \left[ \frac{2 - f_n}{\sqrt{\pi}} (S_{\infty} \sin \eta) + \frac{f_n}{2} \sqrt{\frac{T_b}{T_{\infty}}} \right] e^{-(S_{\infty} \sin \eta)^2} + \left[ (2 - f_n) \left( S_{\infty}^2 \sin^2 \eta + \frac{1}{2} \right) + \frac{f_n}{2} \sqrt{\pi} \sqrt{\frac{T_b}{T_{\infty}}} (S_{\infty} \sin \eta) \right] [1 + \operatorname{erf}(S_{\infty} \sin \eta)] \right\} \quad (10)$$

The shear stress on a surface from free-molecule flow theory is (ref. 7):

$$\tau = f_t \frac{\rho_\infty V_\infty^2 \cos \eta}{2\sqrt{\pi} S_\infty} \left\{ e^{-(S_\infty \sin \eta)^2} + \sqrt{\pi} (S_\infty \sin \eta) [1 + \operatorname{erf}(S_\infty \sin \eta)] \right\} \quad (11)$$

The free-molecule calculations were done for  $M_\infty = 12.3$ ,  $\gamma_\infty = 1.43$ ,  $T_b/T_\infty = 3$ , and  $f_n = f_t = 1$  (completely diffuse reflection). The pressure and shear stresses were converted to forces (acting on the various surfaces of the hexagonal prism) and these forces were summed to find the resultant forces in the axes directions.

Modified Newtonian theory and free-molecule flow theory are the limiting theories for continuum and completely rarefied flow, respectively. No rigorous theory was available for this shape body in the transition flow regime. Therefore, the following semiempirical bridging theory, for predicting aerodynamic coefficients in the transition regime (ref. 8), was used:

$$C_{TR} = \frac{C_{MN} + \frac{M_\infty}{\sqrt{NRe_{\infty,L}}} C_{FM}}{1 + \frac{M_\infty}{\sqrt{NRe_{\infty,L}}}} \quad (12)$$

The appropriate reference length  $L$  for use in this equation is not apparent. However, on short blunt bodies, the decision is not critical; and in the present studies, the length of the hexagonal prism was used. In equation (12), note that for higher Reynolds numbers (continuum flow),  $C_{TR} \approx C_{MN}$ , whereas for low Reynolds number flows (nearer free-molecule flow),  $C_{TR} \approx C_{FM}$ . Other bridging theories are available (refs. 8 and 20); however, this theory was in better agreement with the present data and was also simpler to apply.

## PRESENTATION OF DATA

The experimental force and moment data obtained in this study are presented in table III and in figures 7 to 10. The data are compared with theoretical predictions from modified Newtonian theory, free-molecule theory, and the semiempirical transition bridging theory.

Figure 7 presents  $C_N$ ,  $C_A$ ,  $C_D$ ,  $C_L$ ,  $F_L/F_D$ , and  $C_m$  for the basic hexagonal prism over an angle-of-attack range of  $0^\circ$  to  $90^\circ$  for  $\psi = 0^\circ$ . Figure 8 presents  $C_Y$ ,  $C_A$ ,  $C_D$ ,  $C_C$ ,  $F_C/F_D$ , and  $C_n$  for the basic hexagonal prism over an angle-of-attack range of  $0^\circ$  to  $90^\circ$  for  $-\psi = 90^\circ$ . Figure 9 presents  $C_Y$ ,  $C_N$ ,  $C_D$ ,  $C_C$ ,  $F_C/F_D$ , and  $C_l$  for the basic hexagonal prism over a roll-angle range of  $0^\circ$  to  $-180^\circ$  for  $\sigma = 90^\circ$ .

Figure 10 presents  $C_Y$ ,  $C_N$ ,  $C_D$ ,  $C_C$ ,  $F_C/F_D$ , and  $C_L$  for the simulated ablated hexagonal prism over a roll-angle range of  $0^\circ$  to  $-180^\circ$  for  $\sigma = 90^\circ$ .

Data taken with the sting balance alined with the free-stream flow direction are shown as shaded symbols. These data are believed to have minimum sting-interference effects according to information found in reference 18. Data taken with the sting not alined with the flow are identified with different symbols.

## DISCUSSION OF RESULTS

The longitudinal-force coefficients at  $\psi = 0^\circ$  (figs. 7(a) to 7(e)) exhibit a smooth trend over the  $0^\circ$  to  $90^\circ$  range. The normal-, axial-, and drag-force coefficients (figs. 7(a) to 7(c)) are affected by flow rarefaction in the form of increased force coefficients over that predicted for continuum flow. They agree with the prediction of the transition bridging theory within one standard deviation in most cases and within the maximum uncertainty of the data in all cases.

The lift coefficient (fig. 7(d)) is in better agreement, however, with the modified Newtonian theory than with the bridging theory. This result is not inconsistent with the better agreement of the normal-, axial-, and drag-force coefficients with the bridging theory; instead, it is a result of resolving the force coefficients into the wind-axis system. For example, the experimental normal-force coefficient at  $\sigma = 60^\circ$  is larger than the bridging theory estimate whereas the axial-force coefficient at  $\sigma = 60^\circ$  is smaller than the bridging theory estimate. Now,

$$C_L = C_N \cos \sigma - C_A \sin \sigma \quad (13)$$

and the difference between theory and experiment is magnified in  $C_L$  since a "too small" number relative to the bridging theory estimate (the experimental  $C_A \sin \sigma$ ) is subtracted from a "too large" number relative to the bridging theory estimate (the experimental  $C_N \cos \sigma$ ). However, the drag coefficient data (fig. 6(c)) agree more closely with the bridging theory estimates at  $\sigma = 60^\circ$  than do the lift coefficient data since

$$C_D = C_N \sin \sigma + C_A \cos \sigma \quad (14)$$

and the difference between theory and experiment is compensated to some extent in  $C_D$  since a too small number is added to a too large number. Of course, the magnitude of the angle of attack affects the results, as can be seen from equations (13) and (14). The resolution of this "apparent inconsistency" presents a strong case for examining the agreement between theoretical and experimental force data in two axes systems since discrepancies may be more apparent in one system than in another system.

Also in figure 7(d), the negative lift coefficients at the lower angles of attack are not predicted by free-molecule theory. Since the lift coefficient data are in better agreement with modified Newtonian theory and the drag coefficient data with the bridging theory, the lift-drag ratio ( $F_L/F_D$ , fig. 7(e)) distribution falls between the predictions of these two methods.

The effects of sting interference on pitching-moment coefficient are shown in figure 7(f). The data connected with the dashed lines were taken with a particular model mounted on the sting balance, and the various symbols denote sting inclination angle relative to the flow direction. (See the chart in fig. 7(f).) Data taken with each sting inclination angle may be used to form a unique moment curve; sting interference effects are thus indicated. The wide spread in the pitching moments obtained with different sting alignments at approximately the same angle of attack also indicates strong sting interference effects.

Only the moment data taken with the sting aligned with the flow (solid symbols) are presented in figure 7(g) since sting interference effects are believed to be negligible in this orientation (based on the results of ref. 18). The fairing of the data indicates trim points ( $C_m = 0$ ) at  $\sigma = 0^\circ$ ,  $20^\circ$ ,  $38^\circ$ , and  $90^\circ$ , those at  $\sigma = 20^\circ$  and  $\sigma = 90^\circ$  being stable ( $dC_m/d\sigma < 0$ ). The  $90^\circ$  trim point is the more stable of the two (more negative  $dC_m/d\sigma$ ) and is the orientation (from static considerations) that the hexagonal prism would tend to seek during reentry.

The lateral aerodynamic force data (for  $-\psi = 90^\circ$ ) shown in figures 8(a) to 8(e) are very similar to the longitudinal data. The data are very smooth over the entire angle-of-attack range ( $0^\circ$  to  $90^\circ$ ) and are generally in better agreement with the transition bridging theory than with either of the limiting theories. However, the crosswind data (fig. 8(d)) tend to agree with modified Newtonian theory for  $\sigma < 40^\circ$ .

The yawing-moment data (with a side flat facing the flow) (fig. 8(f)) exhibit trends similar to the pitching-moment data (with an apex facing the flow). Stable trim points are at approximately  $15^\circ$  and  $90^\circ$  with the more stable orientation occurring at  $\sigma = 90^\circ$ . Apparently then, the hexagonal prism will, upon reentry, tend to seek the vertical position, that is,  $\sigma = 90^\circ$ , whether an apex ( $\psi = 0^\circ$ ) or a side flat ( $-\psi = 90^\circ$ ) is facing into the flow.

The roll tests were undertaken to determine which of these orientations would occur and the results are presented in figure 9. These tests were conducted with  $\sigma = 90^\circ$  with force data taken from  $-\psi = 0^\circ$  to  $30^\circ$ . The remaining data points in figure 9 (for  $-\psi = 30^\circ$  to  $180^\circ$ ) were calculated from the experimental roll data by use of model symmetry.

The side-force coefficient (fig. 9(a)) is predicted generally very well by the bridging theory. The dip in the data near  $-\psi = 90^\circ$  may possibly be caused by sting interference effects. This dip appears to be inconsistent since the data near  $-\psi = 90^\circ$  were cal-

culated from the data obtained at  $-\psi = 31.3^\circ$ , where the experimental  $C_Y$  data point agrees quite well with the estimate of the bridging theory. Again, this "apparent inconsistency" may be resolved by examining the data and theory in both the wind- and body-axes systems. Near  $-\psi = 30^\circ, 90^\circ$ , and  $150^\circ$ , the  $C_C$  data (fig. 9(d)) show scatter about the bridging theory estimates whereas the  $C_D$  data (fig. 9(c)) are consistently less than the bridging theory estimates. Now

$$C_Y = C_C \cos|\psi| + C_D \sin|\psi| \quad (15)$$

If the experimental crosswind force coefficient  $C_C$  is greater than the estimate of the bridging theory, the difference between the theoretical and experimental values of  $C_Y$  is diminished. If the experimental crosswind force coefficient is less than the estimate of the bridging theory, the difference is magnified. However, the magnitude of the roll angle also affects these results; near  $-\psi = 90^\circ$ ,  $C_Y = C_D$  and hence, there is a dip in the experimental  $C_Y$  data at this roll angle.

Note also the "apparent agreement" of the experimental  $C_Y$  data where  $\epsilon = -8.5^\circ$  and  $-16.4^\circ$  with the bridging theory prediction in figure 9(a). However, the crosswind data (fig. 9(d)) at these same sting inclination angles do not agree with the bridging theory prediction. Again, the importance of making the comparison between theoretical and experimental force data in two axes systems is emphasized.

The normal-force coefficient (fig. 9(b)) is also well predicted by the transition bridging theory with the exception again of some data points taken with the sting balance at an angle to the flow direction. The same remarks apply for the drag-coefficient data in figure 9(c).

Sting interference effects are most noticeable in the crosswind-force-coefficient data and the crosswind-drag ratio in figures 9(d) and 9(e). These effects are enhanced by the small magnitudes of the forces involved as was true in the cases of the longitudinal and lateral moment data. Data taken with the sting balance aligned with the flow (solid symbols) are in reasonable agreement with the predictions of both the bridging theory and modified Newtonian theory.

The rolling-moment data are shown in figure 9(f). Stable trim points appear to exist only at  $-\psi = 30^\circ, 90^\circ$ , and  $150^\circ$ , that is, with a side flat of the hexagonal prism facing into the flow. However, since only two rolling-moment data points were measured ( $-\psi = 0^\circ$  and  $15^\circ$ ), the faired curve must be used with caution. Rolling moment taken on the same shape at  $M_\infty = 3.52$  and  $N_{Re,\infty} = 3.28 \times 10^6$  per meter and tabulated in reference 21 indicate stable trim points with either an apex or a side flat of the basic hexagonal prism facing the flow.

Since the distance from the center of the hexagonal cross section to the side flat is the minimum radius, tests were conducted on a hexagonal prism with one of the six side

flats modified to simulate an ablated flat. The side- and normal-force coefficients and the drag coefficients are presented in figures 10(a) to 10(c). Generally, the data lie between the predictions of the bridging theory and modified Newtonian theory with the zero sting alignment data agreeing more closely with the transition bridging theory.

Sting interference effects may be noted in the crosswind-force coefficient data and the crosswind-drag ratio in figures 10(d) and 10(e). The zero sting alignment data lie very nearly coincident with the bridging theory prediction.

The rolling-moment data for the modified hexagonal prism was taken with the balance moment center located at a point corresponding to the center of gravity of the basic (unmodified) hexagonal prism. This procedure is proper for determining the stability of the fuel cell which contains a very dense core surrounded by the lightweight graphite heat shield. Ablation of the fuel-cell heat shield would shift the center of volume to a much greater degree than the center of gravity. Of course, the data, as measured, would not describe the stability of a hexagonal prism of uniform density.

The rolling-moment data are shown in figure 10(f). Data shown as shaded symbols are the present results (sting balance aligned with the flow) at an average Mach number of 12.3 and an average length Reynolds number of 1380. Data shown as open symbols were obtained at a Mach number of 3.52 and a length Reynolds number of 562 000 (ref. 21). A single fairing through both sets of data is presented. A stable trim point occurs at  $-\psi = 30^\circ$ . In this orientation, the simulated ablated flat is perpendicular to the flow direction. It should be noted, however, that tabulated data in reference 21 indicates that if an apex should ablate (rather than a side flat), the hexagonal prism would be stable with the ablated apex facing the flow.

The results of the longitudinal, lateral, and roll tests on the basic hexagonal prism and the modified (simulated ablated) hexagonal prism indicate that the reentering body will tend to seek the  $90^\circ$  angle-of-attack orientation. In addition, if a side flat starts to ablate, the side-on orientation will remain stable with respect to the center of gravity of the basic hexagonal prism as ablation continues. Thus, any design for the survival of the hexagonal prism fuel cell should consider the heat load for constant orientation, ablation occurring primarily on one side of the prism.

## CONCLUSIONS

The results of aerodynamic force and moment tests on a regular hexagonal prism at an average Mach number of 12.3, an average length Reynolds number of 1380, and a simulated altitude (based on the ratio of unit Reynolds number to Mach number) of 77.7 kilometers referenced to the length of the full-scale body indicated the following conclusions:

1. A semiempirical transition bridging theory, based on continuum and free-molecule limiting theories, agreed well with the experimental aerodynamic force data. The continuum theory (modified Newtonian) and free-molecule theory were found to be inadequate for predicting aerodynamic forces on a hexagonal prism in the transition flow regime.

2. Experimental pitching- and yawing-moment data indicated that the basic hexagonal prism would tend to seek an alinement perpendicular to the flow ( $90^{\circ}$  from end-on) upon reentry. Further tests on a modified (simulated ablated side flat) hexagonal prism indicated that if a side flat started to ablate, the side-on orientation would remain stable with respect to the center of gravity of the unablated hexagonal prism.

3. Sting interference effects were very noticeable on the smaller force data and on the moment data when the sting balance was at an angle to the flow.

Langley Research Center,  
National Aeronautics and Space Administration,  
Hampton, Va., May 18, 1972.

## REFERENCES

1. Spahr, Harold R.; and Larson, David W.: The Multiple Revolution Reentry Problem. AIAA Paper No. 70-989, Aug. 1970.
2. Anon.: U.S. Standard Atmosphere, 1962. NASA, U.S. Air Force, and U.S. Weather Bur., Dec. 1962.
3. Boylan, David E.: Aerodynamic Forces on the Snap-19 Fuel Capsule and Nimbus B Solar Panel at a Simulated High Altitude. AEDC-TR-66-162, U.S. Air Force, Sept. 1966.
4. Stouffer, C. G.: SNAP 19 Capsule Low Reynolds Number Force Test. MND-3607-89 (Contract AT(30-1)-3607), Martin Co., Oct. 1966.
5. Stouffer, C. G.: SNAP 19 Capsule Force and Stability Test Conducted in the NASA Langley 31-Inch Continuous Flow Hypersonic Tunnel at Mach 10. MND-3607-90 (Contract AT(30-1)-3607), Martin Co., Dec. 1966.
6. Lees, Lester: Hypersonic Flow. Fifth Int. Aeronaut. Conf. (Los Angeles, Calif.), Inst. Aeronaut. Sci., Inc., June 1955, pp. 241-276.
7. Hayes, Wallace D.; and Probstein, Ronald F.: Hypersonic Flow Theory. Academic Press, Inc., 1959.
8. Blick, Edward F.: Aerodynamic Coefficients in the Slip and Transition Regime. AIAA J., vol. 1, no. 11, Nov. 1963, pp. 2656-2658.
9. Tobak, Murray; and Schiff, Lewis B.: A Nonlinear Aerodynamic Moment Formulation and Its Implications for Dynamic Stability Testing. AIAA Paper No. 71-275, Mar. 1971.
10. Mechtly, E. A.: The International System of Units - Physical Constants and Conversion Factors (Revised). NASA SP-7012, 1969.
11. Guy, Robert W.: A Calibration and Diagnosis of the Test Stream of an Electric Arc-Heated Wind Tunnel. M.A.E. Thesis, Univ. of Virginia, Sept. 1969.
12. Lordi, J. A.; Mates, R. E.; and Moselle, J. R.: Computer Program for the Numerical Solution of Nonequilibrium Expansions of Reacting Gas Mixtures. Rep. No. AD-1689-A-6 (Contract No. NASr-109), Cornell Aeron. Lab., Inc., Oct. 1965.
13. Burke, A. F.; and Bird, K. D.: The Use of Conical and Contoured Expansion Nozzles in Hypervelocity Facilities. Rep. No. CAL-112, Cornell Aero. Lab., Inc., Mar. 1962. (Rev. July 1962.)

14. Boatright, W. B.; Stewart, R. B.; and Sebacher, D. I.: Testing Experience and Calibration Experiments in a Mach Number 12, 1-Foot Hypersonic Arc Tunnel. Third Hypervelocity Techniques Symposium, Univ. of Denver and Arnold Eng. Develop. Center, Mar. 1964, pp. 182-212.
15. Daum, F. L.; Shang, J. S.; and Elliott, G. A.: Impact Pressure Behavior in Rarefied Hypersonic Flow. AIAA J., vol. 3, no. 8, Aug. 1965, pp. 1546-1548.
16. White, Richard B.: Hypersonic Viscous-Interaction and Rarefaction Effects on Impact Probes. AIAA Stud. J., vol. 5, no. 2, Apr. 1967, pp. 46-49.
17. Guy, R. W.; and Winebarger, R. M.: Effect of Orifice Size and Heat Transfer Rate on Measured Static Pressures in a Low-Density Arc-Heated Wind Tunnel. NASA TN D-3829, 1967.
18. Stivers, Louis S., Jr.: Effects of A Sting Support on the Supersonic Force and Moment Characteristics of an Apollo Model at Angles From  $-30^{\circ}$  to  $+185^{\circ}$ . NASA TM X-1081, 1965.
19. Baird, D. C.: Experimentation: An Introduction to Measurement Theory and Experiment Design. Prentice-Hall, Inc., c.1962.
20. Matting, F. W.: Approximate Bridging Relations in the Transitional Regime Between Continuum and Free-Molecule Flows. J. Spacecraft, vol. 8, no. 1, Jan. 1971, pp. 35-40.
21. Haar, M. I.: Six Component Supersonic Force and Moment Tests of the Hexagonally-Shaped Snap 19/Pioneer Heat Source. INSD-2873-81, Teledyne Isotopes, July 30, 1971.

TABLE I.- WIND-TUNNEL TEST CONDITIONS

Test	$P_{t,1}$ , N/m <sup>2</sup>	$T_{t,1}$ , K	$H_{t,1}$ , Mj/kg	$T_{\infty}$ , K	$\rho_{\infty}$ , kg/m <sup>3</sup>	$V_{\infty}$ , m/sec	$P_{\infty}$ , N/m <sup>2</sup>	$q_{\infty}$ , N/m <sup>2</sup>	$P_{t,2}$ , N/m <sup>2</sup>	$\gamma_{\infty}$	$M_{\infty}$	$N_{Re,\infty,L}$	$N_{Re,\infty/m}$	$\bar{V}_{\infty,L}$	$\lambda_{\infty}$ , cm
1	$7.76 \times 10^5$	3910	6.09	150	$1.15 \times 10^{-4}$	3060	5.23	537	987	1.42	12.0	1460	$3.42 \times 10^4$	0.314	0.053
2	7.40	3770	5.65	145	1.15	2975	4.99	509	937	1.42	12.0	1480	3.46	.312	.052
3	7.42	3800	5.75	145	1.14	2990	4.98	510	937	1.42	12.0	1410	3.41	.319	.053
4	7.84	3880	6.00	140	1.23	3040	5.65	568	1043	1.42	11.9	1540	3.59	.303	.050
5	7.81	3870	5.95	150	1.20	3040	5.45	553	1016	1.42	12.0	1520	3.54	.308	.042
6	8.41	4280	7.30	160	1.14	3260	5.77	605	1109	1.43	12.1	1440	3.35	.318	.054
7	8.22	4290	7.35	165	1.13	3270	5.80	605	1109	1.43	12.1	1430	3.32	.319	.055
8	8.21	4300	7.40	160	1.12	3275	5.76	602	1105	1.43	12.1	1420	3.31	.321	.055
9	8.12	4280	7.30	165	1.14	3260	5.83	605	1109	1.43	12.0	1430	3.33	.317	.054
10	8.95	5000	9.37	175	.97	3600	5.53	631	1154	1.45	12.6	1280	2.99	.352	.064
11	9.02	5040	9.44	170	.97	3620	5.50	631	1154	1.45	12.6	1270	2.97	.353	.064
12	8.91	4940	9.12	170	1.00	3570	5.63	637	1166	1.44	12.5	1310	3.06	.345	.062
13	9.19	5400	10.47	180	.88	3770	5.27	629	1148	1.45	12.8	1190	2.78	.356	.070
14	8.87	4880	9.02	170	1.02	3545	5.69	637	1166	1.44	12.5	1320	3.08	.343	.061
15	9.31	5400	10.47	180	.88	3775	5.22	627	1145	1.45	12.9	1190	2.77	.373	.071
16	8.98	5060	9.51	170	.94	3625	5.30	616	1127	1.45	12.7	1250	2.92	.359	.066
17	7.70	3930	6.14	150	1.12	3070	5.10	528	970	1.42	12.1	1440	3.36	.318	.054
18	7.93	4040	6.51	155	1.11	3135	5.20	545	1001	1.42	12.1	1430	3.33	.319	.055
19	7.97	4040	6.51	150	1.12	3135	5.26	550	1010	1.42	12.1	1440	3.35	.318	.054
20	8.15	4200	7.09	160	1.14	3220	5.69	591	1084	1.43	12.1	1440	3.22	.318	.057
21	8.13	4130	6.84	160	1.16	3180	5.68	586	1076	1.43	12.0	1460	3.40	.313	.053
22	9.06	4920	9.14	170	1.02	3560	5.77	648	1186	1.44	12.5	1330	3.11	.342	.061
23	8.88	4940	9.21	175	1.02	3570	5.78	648	1186	1.44	12.5	1320	3.09	.343	.061
24	8.91	4800	8.84	170	1.05	3510	5.87	648	1186	1.44	12.4	1360	3.16	.336	.059
25	7.97	4080	6.65	150	1.10	3160	5.20	547	1004	1.42	12.2	1400	3.29	.325	.056
26	8.98	4870	9.00	170	.98	3540	5.37	614	1123	1.44	12.6	1300	3.03	.349	.063
27	8.81	4760	8.72	170	1.02	3500	5.57	622	1138	1.44	12.5	1330	3.10	.342	.061
28	8.90	4790	8.79	170	1.01	3500	5.54	622	1139	1.44	12.5	1320	3.09	.343	.061
29	8.90	4700	8.54	170	1.03	3460	5.58	622	1138	1.44	12.4	1350	3.14	.337	.060
30	8.70	4640	8.37	170	1.06	3440	5.74	627	1148	1.44	12.3	1360	3.18	.334	.058
31	8.95	4670	8.47	170	1.04	3450	5.61	622	1140	1.44	12.4	1360	3.17	.336	.059
32	8.70	4620	8.33	170	1.06	3430	5.68	621	1138	1.44	12.3	1360	3.18	.333	.058
33	7.71	3940	6.19	150	1.12	3075	5.12	530	974	1.42	12.1	1440	3.35	.318	.054
34	7.60	3900	6.05	150	1.13	3050	5.09	525	965	1.42	12.1	1450	3.38	.317	.054
35	8.61	4750	8.68	170	1.01	3490	5.51	613	1123	1.44	12.4	1320	3.07	.341	.061
36	8.74	4790	8.68	170	1.01	3490	5.65	614	1123	1.44	12.4	1320	3.07	.341	.061
37	8.67	4780	8.77	170	1.01	3500	5.51	617	1129	1.44	12.5	1320	3.07	.343	.062
38	7.76	3930	6.14	150	1.11	3070	5.02	523	961	1.42	12.1	1440	3.35	.318	.054
39	7.62	3900	6.07	150	1.14	3050	5.15	530	973	1.42	12.0	1460	3.40	.313	.053
40	7.97	4070	6.63	150	1.10	3150	5.21	547	1004	1.42	12.2	1420	3.30	.323	.056
41	7.57	3970	6.29	150	1.10	3090	5.07	526	965	1.42	12.1	1410	3.29	.322	.055
42	7.97	4090	6.68	155	1.10	3160	5.29	554	1017	1.43	12.1	1420	3.31	.320	.055
43	7.57	3900	6.06	150	1.12	3055	5.07	523	961	1.42	12.1	1440	3.36	.318	.054
44	7.57	3880	6.00	150	1.12	3040	5.02	519	953	1.42	12.1	1440	3.36	.318	.054
45	7.63	3920	5.82	150	1.15	3010	5.04	518	953	1.42	12.0	1480	3.45	.312	.052
46	8.90	4870	9.00	170	.99	3540	5.49	622	1139	1.44	12.5	1310	3.05	.345	.062
47	8.91	4850	8.96	170	1.00	3530	5.50	622	1139	1.44	12.5	1310	3.06	.345	.062
48	8.88	5040	9.44	175	.96	3620	5.49	628	1148	1.45	12.6	1270	2.95	.353	.065
49	8.92	4780	8.77	170	1.00	3500	5.46	616	1127	1.44	12.5	1320	3.08	.343	.061

TABLE II.- RANDOM-ERROR ANALYSIS

(a) Longitudinal data.  $\psi = 0^\circ$

$\sigma$ , deg	Error type (a)	Percent of -					$\sigma$ , deg	Error type (a)	Percent of -
		C <sub>N</sub>	C <sub>A</sub>	C <sub>L</sub>	C <sub>D</sub>	F <sub>L</sub> /F <sub>D</sub>			C <sub>m</sub>
0.1	1	760	6	270	6	270	0.2	1	47
	2	1300	13	510	13	500		2	76
15	1	10	6	8	6	9	15	1	29
	2	25	13	18	13	20		2	48
45	1	4	5	5	5	5	30	1	8
	2	11	13	11	11	11		2	17
75	1	4	8	4	4	4	45	1	7
	2	9	22	10	9	9		2	14
60	1						60	1	4
	2							2	9
75	1						75	1	5
	2							2	10
90	1						90	1	41
	2							2	67

(b) Lateral data.  $-\psi = 90^\circ$

$\sigma$ , deg	Error type (a)	Percent of -					$\sigma$ , deg	Error type (a)	Percent of -
		C <sub>Y</sub>	C <sub>A</sub>	C <sub>C</sub>	C <sub>D</sub>	F <sub>C</sub> /F <sub>D</sub>			C <sub>n</sub>
0.1	1	230	6	550	6	550	0.1	1	39
	2	400	13	1000	13	1000		2	64
15	1	9	6	7	6	8	25	1	7
	2	23	12	17	12	19		2	15
45	1	5	5	5	5	5	40	1	7
	2	11	12	13	11	13		2	15
75	1	5	10	4	5	4	60	1	5
	2	10	27	11	10	10		2	11
85	1						85	1	510
	2							2	770

(c) Roll data.  $\sigma = 90^\circ$

$-\psi$ , deg	Error type (a)	Percent of -					$-\psi$ , deg	Error type (a)	Percent of -
		C <sub>Y</sub>	C <sub>N</sub>	C <sub>C</sub>	C <sub>D</sub>	F <sub>C</sub> /F <sub>D</sub>			C <sub>l</sub>
15	1	5	5	13	5	12	0.1	1	410
	2	13	10	30	10	28		2	620
103	1	5	5	14	5	14	15	1	13
	2	13	13	31	11	31		2	25
135	1	5	5	12	5	12	103	1	4
	2	11	11	27	11	27		2	9
135	1						135	1	13
	2							2	24

<sup>a</sup>Error type 1, standard deviation; error type 2, maximum uncertainty.

TABLE III.- TEST RESULTS

(a) Longitudinal data.  $\psi = 0^\circ$

Test	$\sigma$ , deg	$C_N$	$C_A$	$C_L$	$C_D$	$F_L/F_D$	$\theta$ , deg	$\epsilon$ , deg
1	4.2	0.048	0.908	-0.018	0.909	-0.020	0	4.2
	-16.2	-.187	.900	.071	.916	.078		-16.2
2	4.2	0.043	0.931	-0.025	0.932	-0.027	0	4.2
	-2.6	-.025	.919	.017	.919	.018		-2.6
	-7.1	-.077	.958	.042	.959	.044		-7.1
	-11.5	-.133	.954	.060	.961	.062		-11.5
	-12.0	-.145	.953	.056	.962	.058		-12.0
3	0.1	-0.001	0.958	-0.003	0.958	-0.003	0	0.1
	8.4	.083	.956	-.057	.958	-.060		8.4
	-16.3	-.205	.947	.069	.967	.071		-16.3
4	15.2	0.144	0.903	-0.098	0.909	-0.108	15	0.2
	24.1	.328	.903	-.069	.958	-.072		9.1
	-1.6	-.068	.885	-.043	.887	-.048		-16.6
5	6.2	0.034	0.906	-0.064	0.904	0.071	15	-8.8
	14.8	.145	.902	-.091	.909	-.100		-.2
	31.5	.573	.864	.037	1.035	.036		16.5
6	45.2	1.021	0.695	0.226	1.214	0.186	45	0.2
	53.6	1.277	.534	.328	1.344	.244		8.6
7	36.6	0.713	0.875	0.051	1.128	0.046	45	-8.4
	44.9	1.058	.784	.196	1.302	.151		-1
	61.0	1.445	.397	.353	1.456	.242		16.0
8	75.2	1.661	0.164	0.266	1.648	0.161	75	0.2
	83.4	1.707	.077	.119	1.705	.070		8.4
9	66.6	1.567	0.313	0.335	1.562	0.214	75	-8.4
	74.8	1.698	.172	.279	1.683	.166		-.2
	91.4	1.682	-.030	-.012	1.682	-.007		16.4

Test	$\sigma$ , deg	$C_m$	$\theta$ , deg	$\epsilon$ , deg
10	0.2	0.0019	0	0.2
11	15.2	.0043	15	.2
12	30.0	-.0128	30	0
13	45.1	.0253	45	.1
14	60.1	.0424	60	.1
15	75.1	.0365	75	.1
16	90.1	-.0022	90	0

TABLE III.- TEST RESULTS - Continued

(b) Lateral data.  $-\psi = 90^\circ$

Test	$\sigma$ , deg	$C_Y$	$C_A$	$C_C$	$C_D$	$F_C/F_D$	$\theta$ , deg	$\epsilon$ , deg
17	0.1	0.003	0.976	0.001	0.976	0.001	0	0.1
	8.5	.084	.974	-.061	.976	-.062		8.5
	-16.2	-.206	.939	.064	.959	.067		-16.2
18	0.1	-0.001	0.947	-0.003	0.947	-0.003	0	0.1
	8.4	.082	.945	-.056	.947	-.060		8.4
	-15.8	-.203	.936	.059	.956	.062		-15.8
19	4.3	0.040	0.938	-0.030	0.939	-0.032	0	4.3
	-8.0	-.094	.961	.041	.965	.042		-8.0
	-16.1	-.205	.902	.053	.923	.057		-16.1
20	15.1	0.162	0.956	-0.093	0.965	-0.096	15	0.1
	23.9	.328	.912	-.070	.966	-.072		8.9
	-1.6	-.060	.920	-.034	.922	-.037		-16.6
21	6.4	0.033	0.951	-0.073	0.949	-0.077	15	-8.6
	14.9	.144	.945	-.104	.950	-.159		-.1
	31.4	.545	.910	-.009	1.060	-.009		16.4
22	45.1	0.936	0.723	0.149	1.174	0.127	45	0.1
	53.7	1.161	.559	.237	1.266	.187		8.7
23	36.5	0.688	0.912	0.010	1.143	0.009	45	-8.5
	44.9	.938	.751	.134	1.194	.112		-.1
	61.3	1.312	.407	.273	1.346	.203		16.3
24	58.7	1.234	0.497	0.216	1.313	0.165	75	-16.3
	75.1	1.393	.147	.217	1.384	.156		.1
	83.5	1.480	.065	.103	1.478	.070		8.5
25	66.2	1.474	0.339	0.285	1.486	0.192	75	-8.8
	74.9	1.531	.157	.247	1.519	.163		-.1
	91.2	1.519	-.052	.020	1.520	.013		16.2

Test	$\sigma$ , deg	$C_n$	$\theta$ , deg	$\epsilon$ , deg
26	0.1	0.0024	0	0.1
27	25.1	-.0153	25	.1
28	40.0	.0162	40	0
29	60.0	.0305	60	0
30	60.1	.0283	60	.1
31	85.1	-.0002	85	.1
32	85.0	.0002	85	0

TABLE III.- TEST RESULTS - Continued

(c) Roll data for regular hexagonal prism.  $\sigma = 90^\circ$ . (Values above dashed rule are measured data; values below are calculated from the measured values.)

Test	$-\psi$ , deg	$C_Y$	$C_N$	$C_C$	$C_D$	$F_C/F_D$	$\theta$ , deg	$\epsilon$ , deg
33	-1.4	-0.078	1.671	-0.039	1.673	-0.023	15	-16.4
	61.4	1.486	.767	.039	1.673	.023		
	58.7	1.408	.903	-.039	1.673	-.023		
	121.4	1.408	-.903	.039	1.673	.023		
	118.7	1.486	-.767	-.039	1.673	-.023		
	181.4	-.078	-1.671	.039	1.673	.023		
	15.2	0.389	1.591	-0.041	1.638	-0.025	15	0.2
	44.9	1.184	1.133	.041	1.638	.025		
	75.2	1.573	.459	-.041	1.638	-.025		
	104.9	1.573	-.459	.041	1.638	.025		
	135.2	1.184	-1.133	-.041	1.638	-.025		
	164.9	0.389	-1.591	.041	1.638	.025		
	23.7	0.623	1.377	0.017	1.512	0.011	15	8.7
	36.3	.881	1.228	-.017	1.512	-.011		
	83.7	1.504	.149	.017	1.512	.011		
	96.3	1.504	-.149	-.017	1.512	-.011		
143.7	.881	-1.228	.017	1.512	.011			
156.3	.623	-1.377	-.017	1.512	-.011			
34	6.5	0.105	1.731	-0.090	1.732	-0.052	15	-8.5
	53.6	1.447	.957	.090	1.732	.052		
	66.5	1.552	.775	-.090	1.732	-.052		
	113.6	1.552	-.775	.090	1.732	.052		
	126.5	1.447	-.957	-.090	1.732	-.052		
	173.6	.105	-1.731	.090	1.732	.052		
	14.8	0.359	1.614	-0.064	1.652	-0.039	15	-0.2
	45.3	1.219	1.118	.064	1.652	.039		
	74.8	1.577	.497	-.064	1.652	-.039		
	105.3	1.577	-.497	.064	1.652	.039		
	134.8	1.219	-1.118	-.064	1.652	-.039		
	165.3	.359	-1.614	.064	1.652	.039		
	31.3	0.829	1.233	0.068	1.484	0.046	15	16.3
	28.7	.653	1.335	-.068	1.484	-.046		
	91.3	1.482	-.102	.068	1.484	.046		
	88.7	1.482	.102	-.068	1.484	-.046		
151.3	.653	-1.335	.068	1.484	.046			
148.7	.829	-1.233	-.068	1.484	-.046			

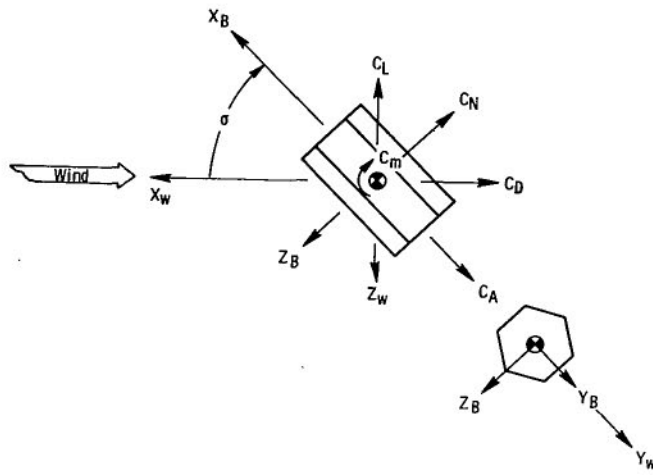
Test	$-\psi$ , deg	$C_L$	$\theta$ , deg	$\epsilon$ , deg
35	0.1	-0.0002	0	0.1
36	15.1	-.0038	15	.1
37	15.2	-.0042	15	.2

TABLE III.- TEST RESULTS - Concluded

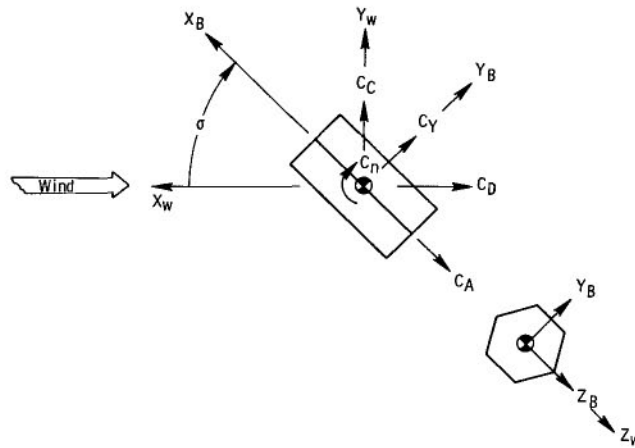
(d) Roll data for simulated ablated hexagonal prism.  $\sigma = 90^\circ$

Test	$-\psi$ , deg	$C_Y$	$C_N$	$C_C$	$C_D$	$F_C/F_D$	$\theta$ , deg	$\epsilon$ , deg
38	15.1	0.507	1.552	0.085	1.631	0.052	15	0.1
	23.7	.705	1.446	.065	1.608	.040		8.6
	-1.1	.081	1.586	.111	1.584	.070		-16.1
39	14.9	0.492	1.589	0.067	1.662	0.040	15	-0.1
	6.5	.278	1.668	.089	1.688	.053		-8.5
	31.2	.838	1.298	.045	1.544	.029		16.2
40	86.8	1.248	0.286	-0.216	1.262	-0.171	103	-16.2
	103.3	1.312	-.375	.065	1.363	.047		.3
	112.1	1.294	-.697	.159	1.462	.109		9.1
41	86.8	1.251	0.285	-0.215	1.265	-0.170	103	-16.2
	103.2	1.365	-.390	.069	1.418	.049		.2
	111.6	1.287	-.676	.156	1.445	.108		8.6
42	94.1	1.260	0.009	-0.099	1.256	-0.079	103	-8.9
	102.9	1.279	-.336	.043	1.322	.033		.1
	119.2	1.106	-.809	.167	1.360	.123		16.2
43	118.1	1.215	-0.674	0.022	1.389	0.016	135	-16.2
	135.2	.934	-1.043	.073	1.398	.052		.2
	143.8	.723	-1.147	.094	1.352	.070		8.8
44	126.4	1.190	-0.905	0.022	1.495	0.015	135	-8.6
	134.9	.997	-1.074	.058	1.464	.039		-.1
	151.4	.528	-1.254	.138	1.354	.102		16.4
45	126.6	1.170	-0.890	0.017	1.469	0.012	135	-8.4
	134.9	.961	-1.037	.058	1.412	.041		.1
	151.2	.491	-1.217	.156	1.303	.120		16.2

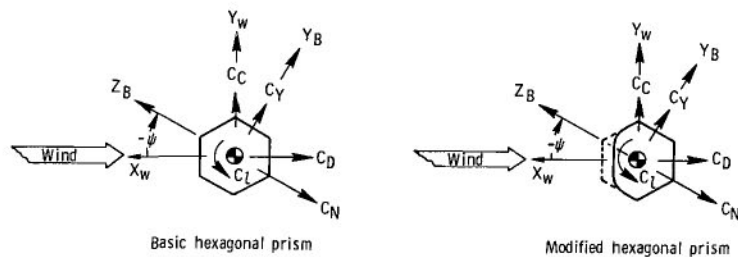
Test	$-\psi$ , deg	$C_L$	$\theta$ , deg	$\epsilon$ , deg
46	15.1	-0.0350	15	0.1
47	103.1	.0397	103	.1
48	103.1	.0413	103	.1
49	135.1	.0094	135	.1



(a) Longitudinal tests.  $\psi = 0^\circ$ .

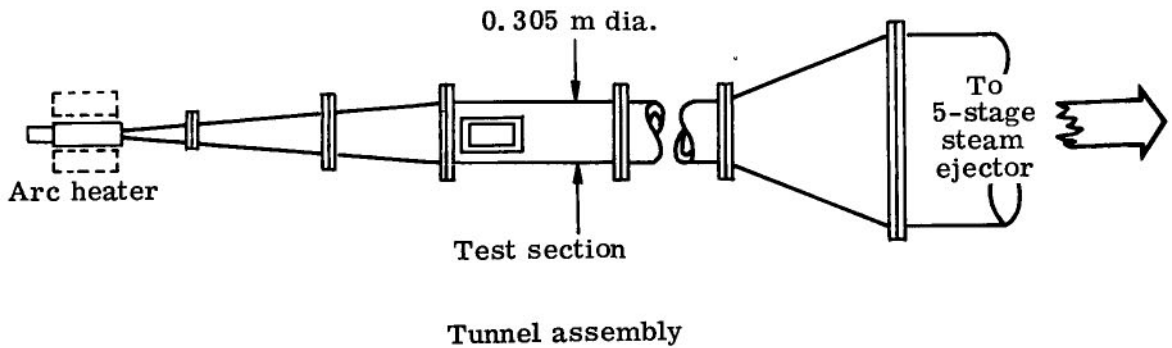
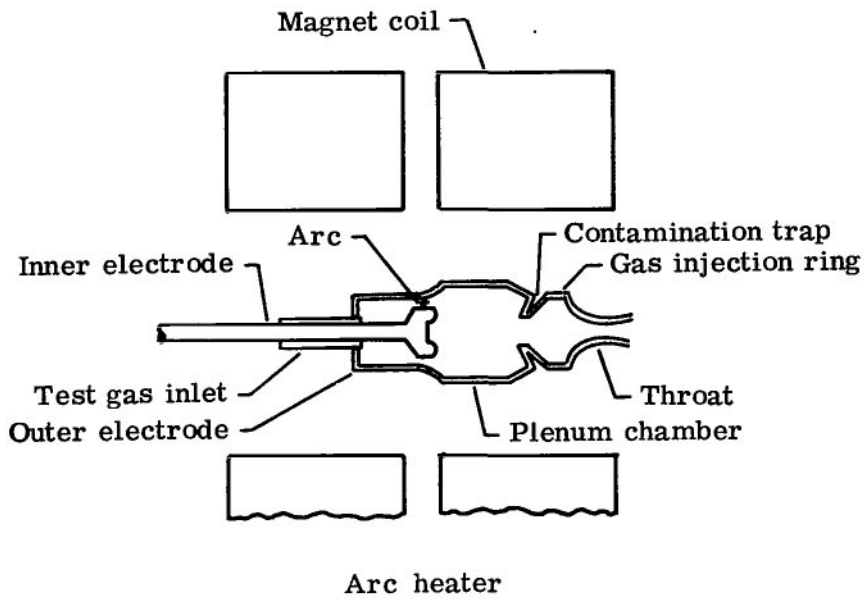


(b) Lateral tests.  $-\psi = 90^\circ$ .



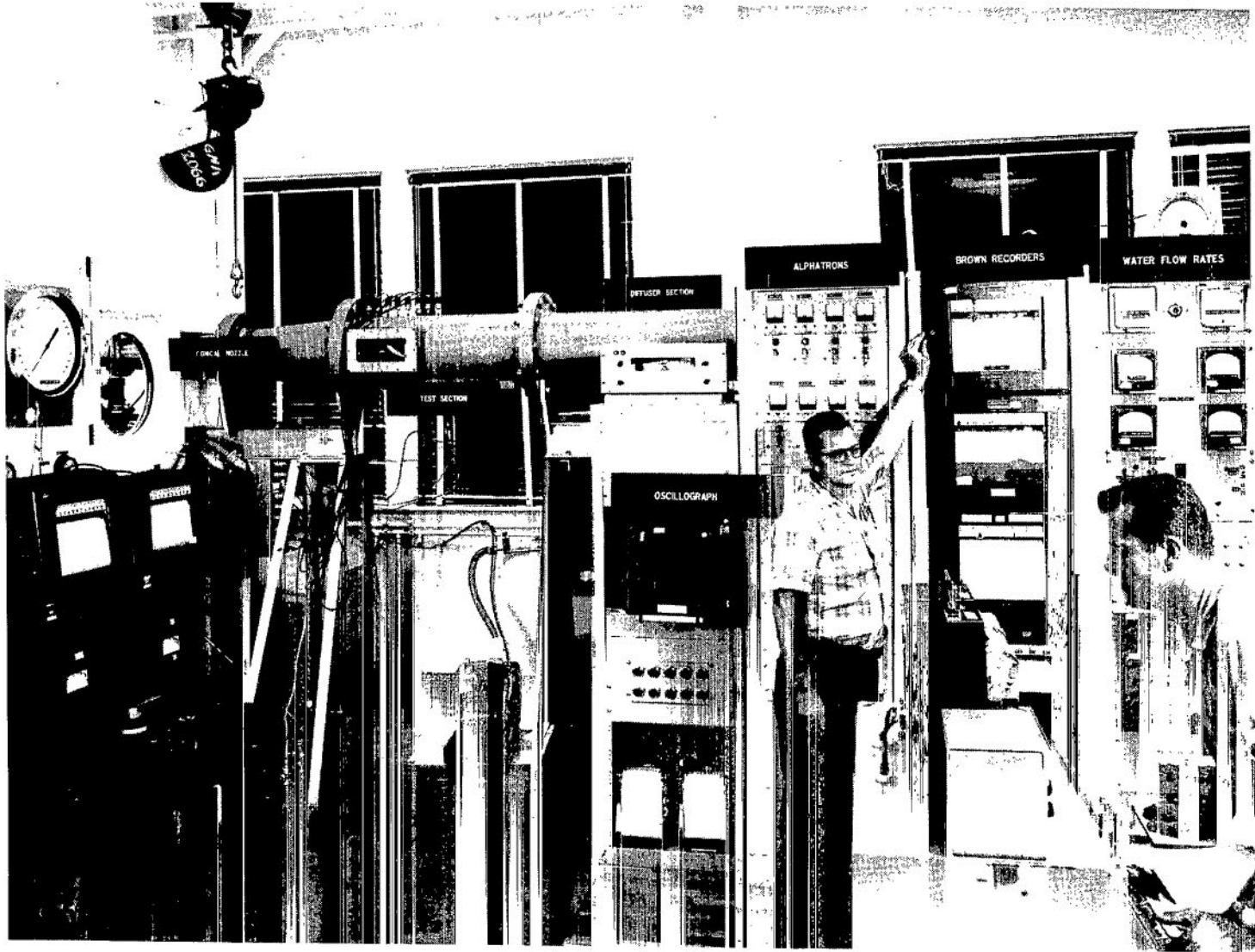
(c) Roll tests.  $\sigma = 90^\circ$ .

Figure 1.- Positive directions of the forces and moments acting on hexagonal prism.



(a) Schematic drawing of the arc heater and the tunnel assembly.

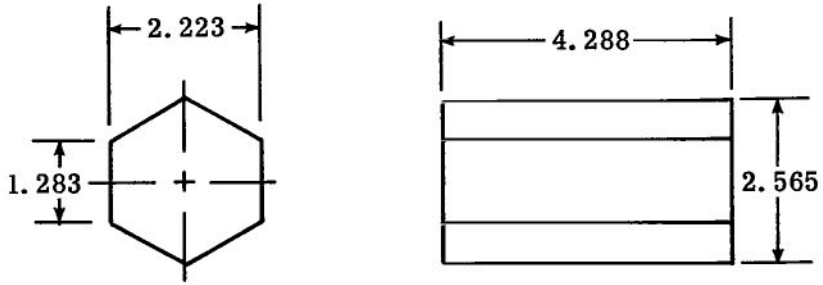
Figure 2.- The 0.305-meter hypersonic arc tunnel at the Langley Research Center.



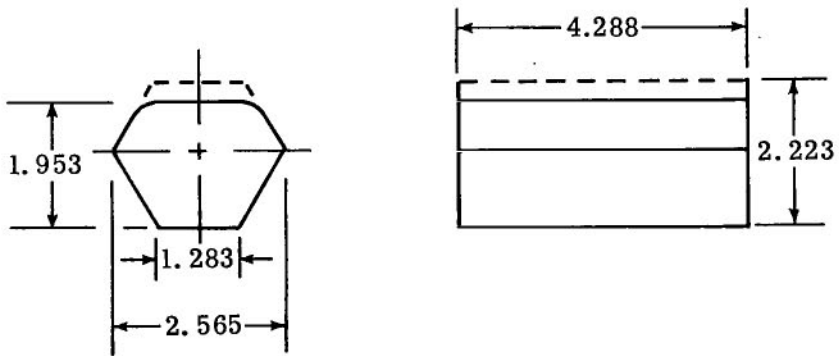
L-63-7232

(b) Arc tunnel and instrumentation.

Figure 2.- Concluded.

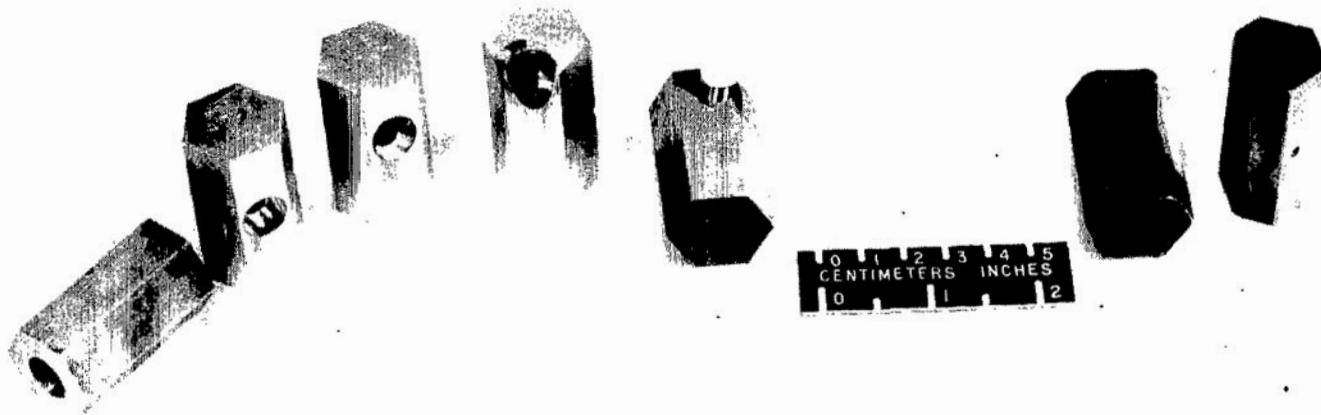


(a) Basic hexagonal prism.



(b) Modified hexagonal prism.

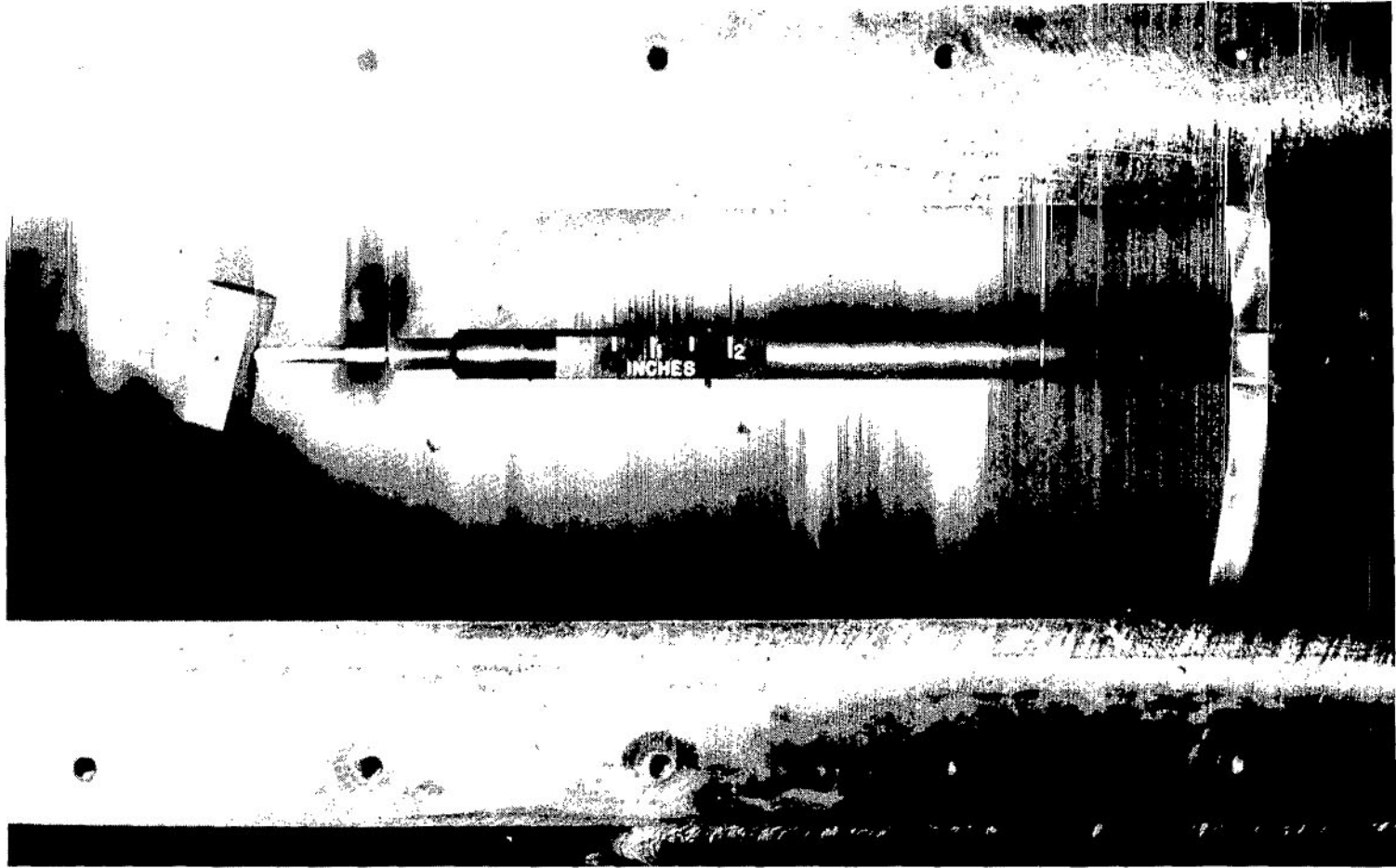
Figure 3.- Geometry of models tested in investigation.  
Dimensions are in centimeters.



L-70-7686

(a) Various hexagonal prism models used during the tests showing the basic and the modified model as well as the balance cavities drilled at different sting offset angles.

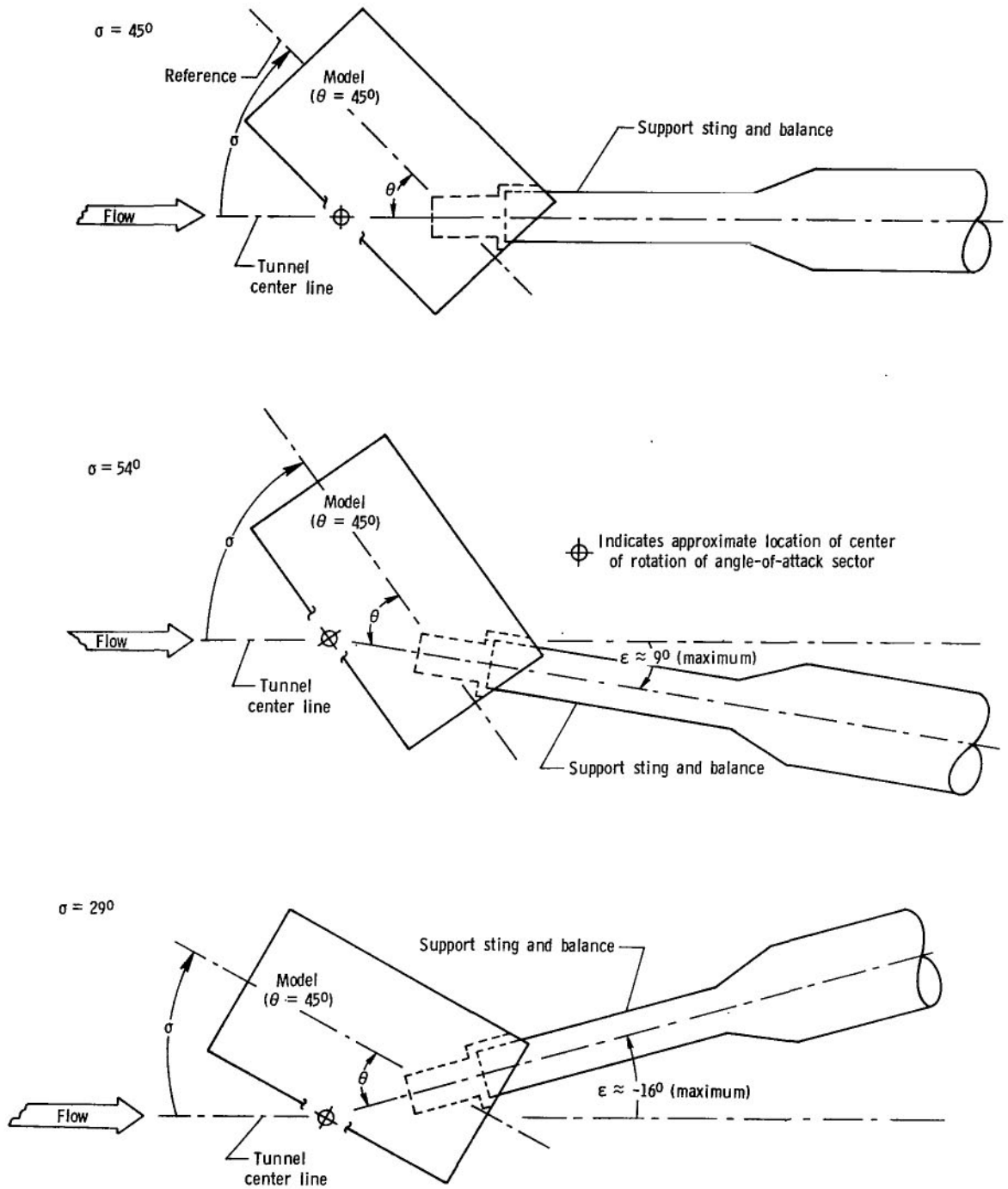
Figure 4.- Typical test models and model attachment in tunnel.



L-70-6608

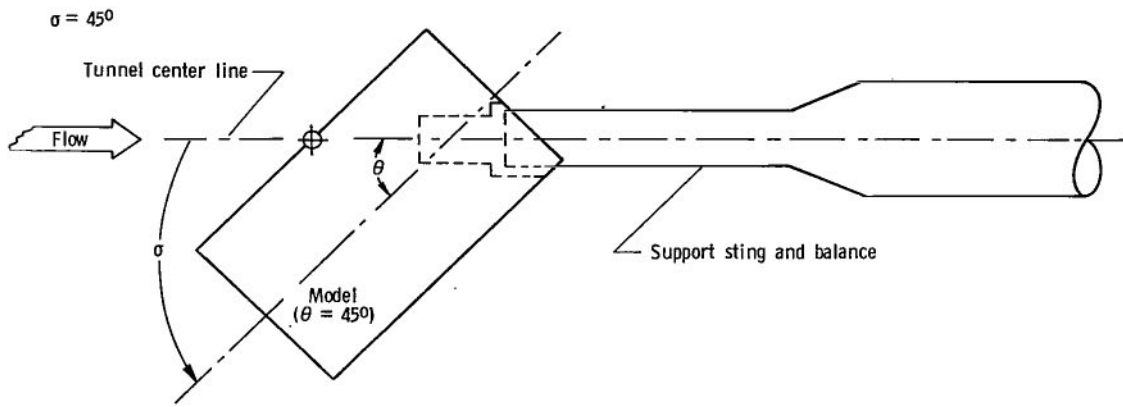
(b) Bottom view of test section showing a hexagonal prism model mounted on the sting balance and the attachment to the tunnel circular-arc section.

Figure 4.- Concluded.

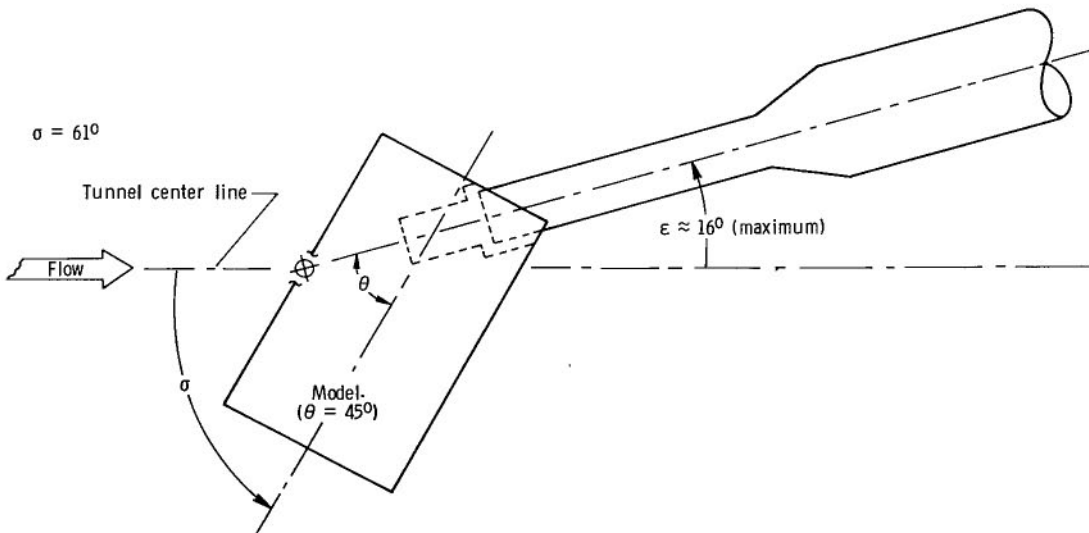
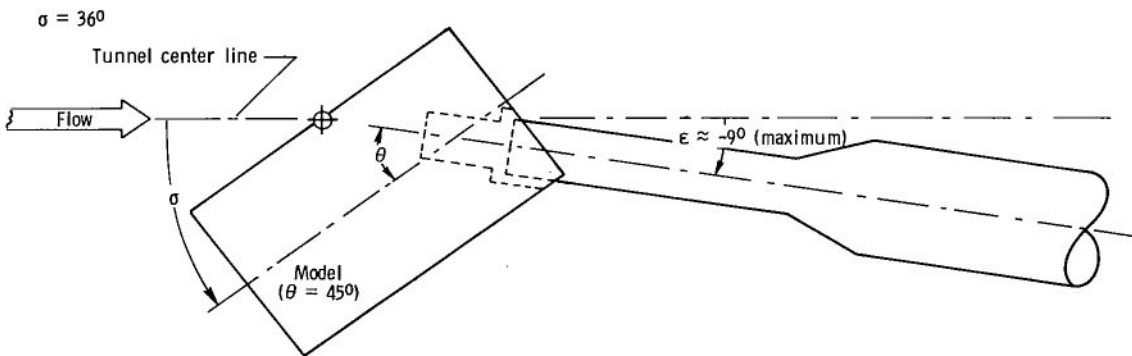


(a) Model balance in normal position.

Figure 5.- Test sequence showing angles of attack attainable with a single model.  
 $\theta = 45^\circ$ .

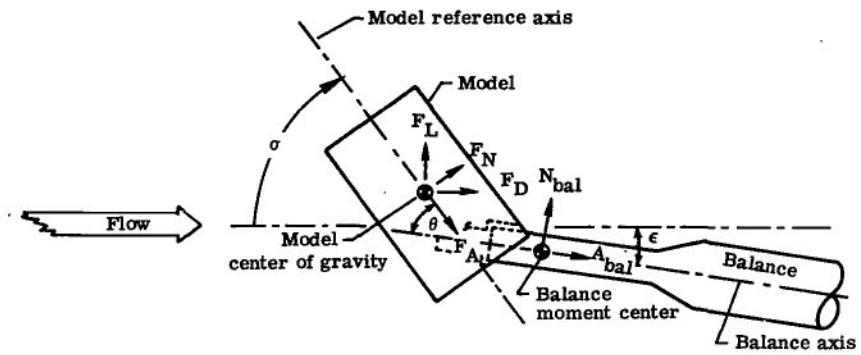


⊕ Indicate approximate location of center of rotation of angle-of-attack sector

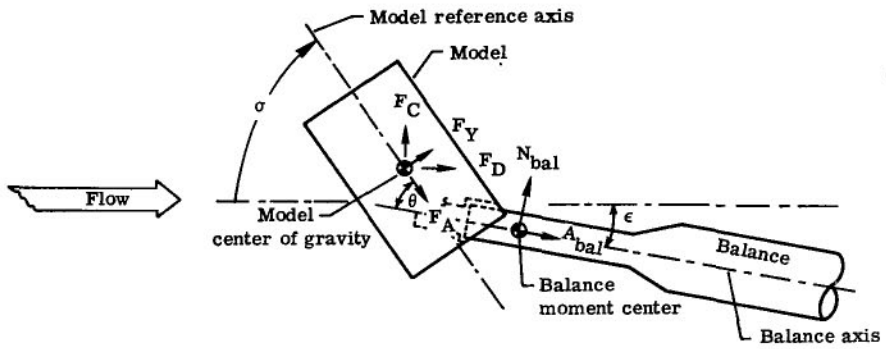


(b) Model balance rotated  $180^\circ$ .

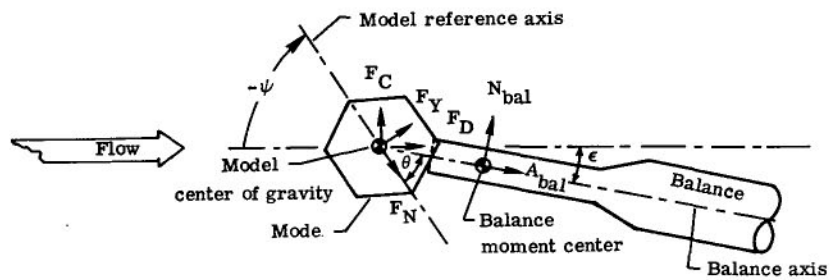
Figure 5.- Concluded.



(a) Longitudinal tests.  $\psi = 0^{\circ}$ .

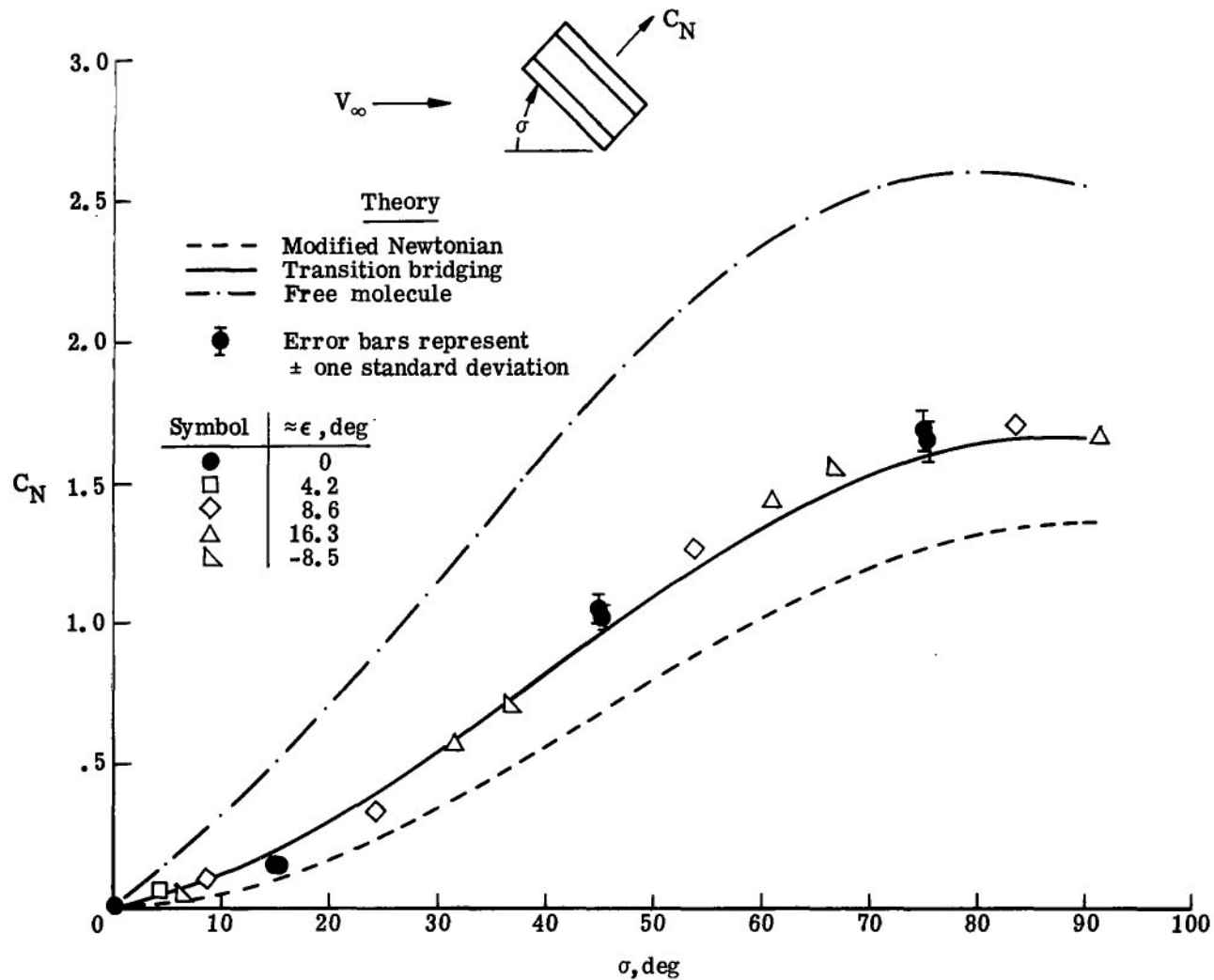


(b) Lateral tests.  $-\psi = 90^{\circ}$ .



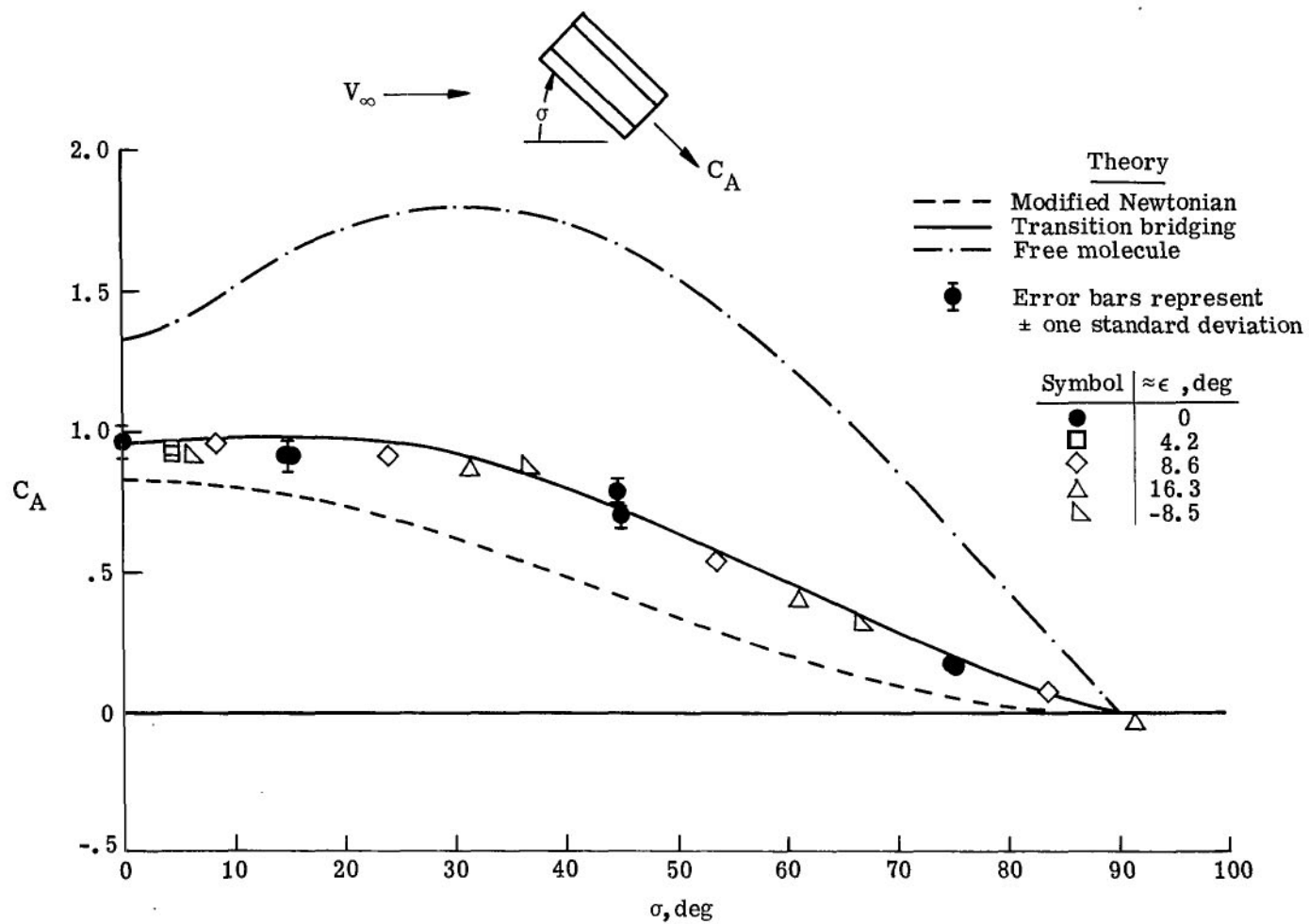
(c) Roll tests.  $\sigma = 90^{\circ}$ .

Figure 6.- Relationship between forces and angles in the balance, body, and wind axes systems.



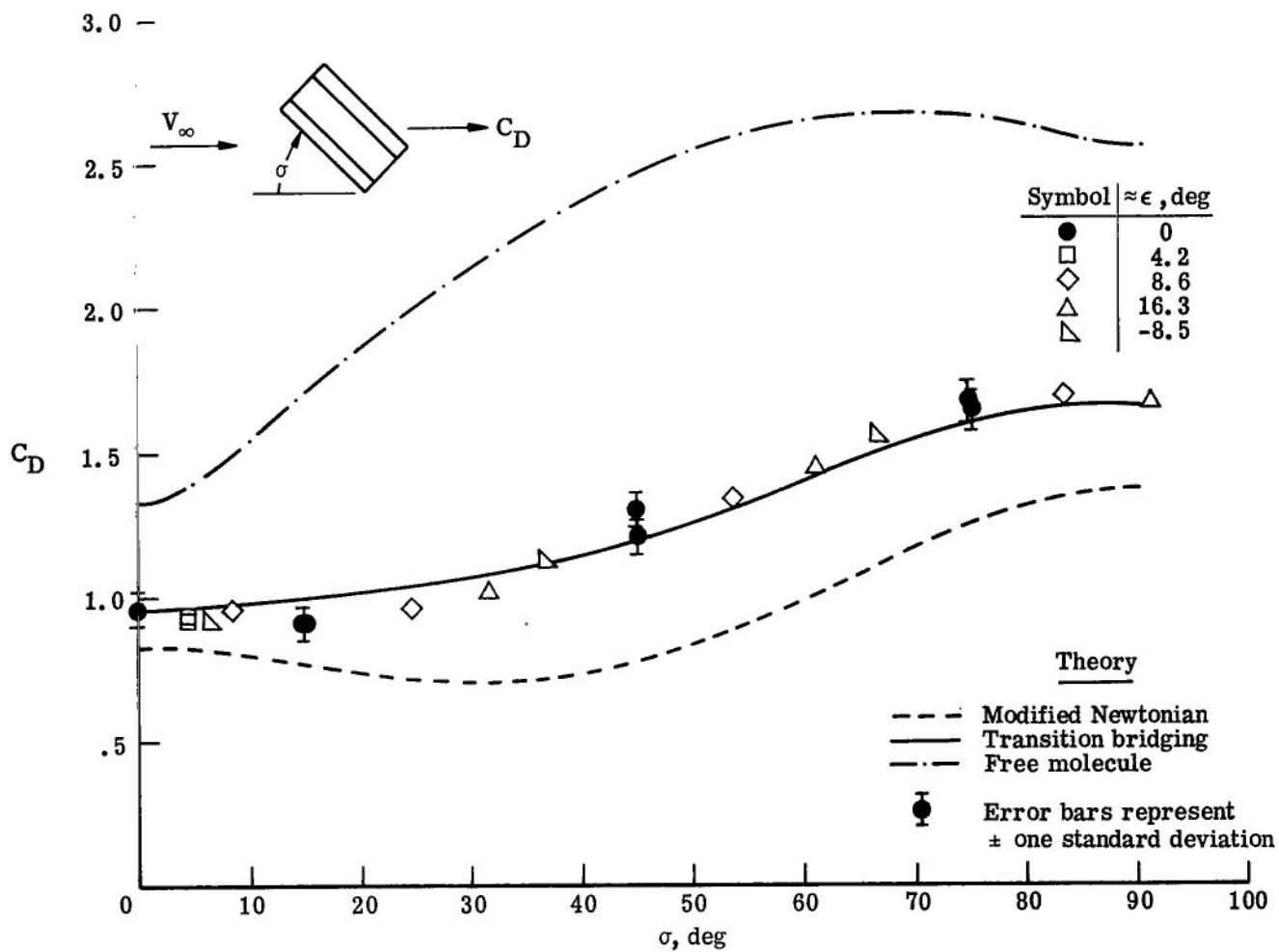
(a) Normal-force coefficient.

Figure 7.- Longitudinal aerodynamic characteristics of a hexagonal prism.  $\psi = 0^\circ$ .



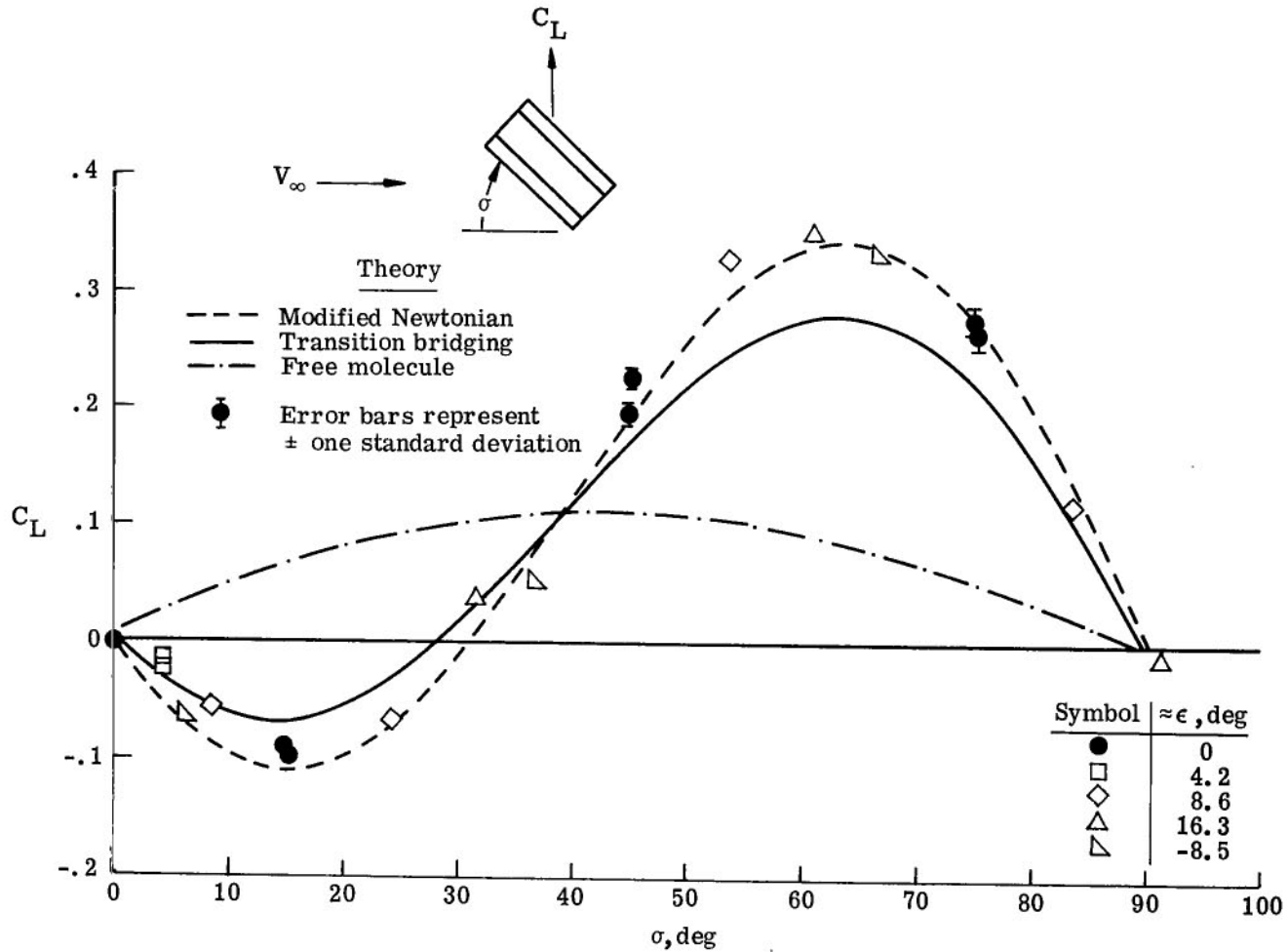
(b) Axial-force coefficient.

Figure 7.- Continued.



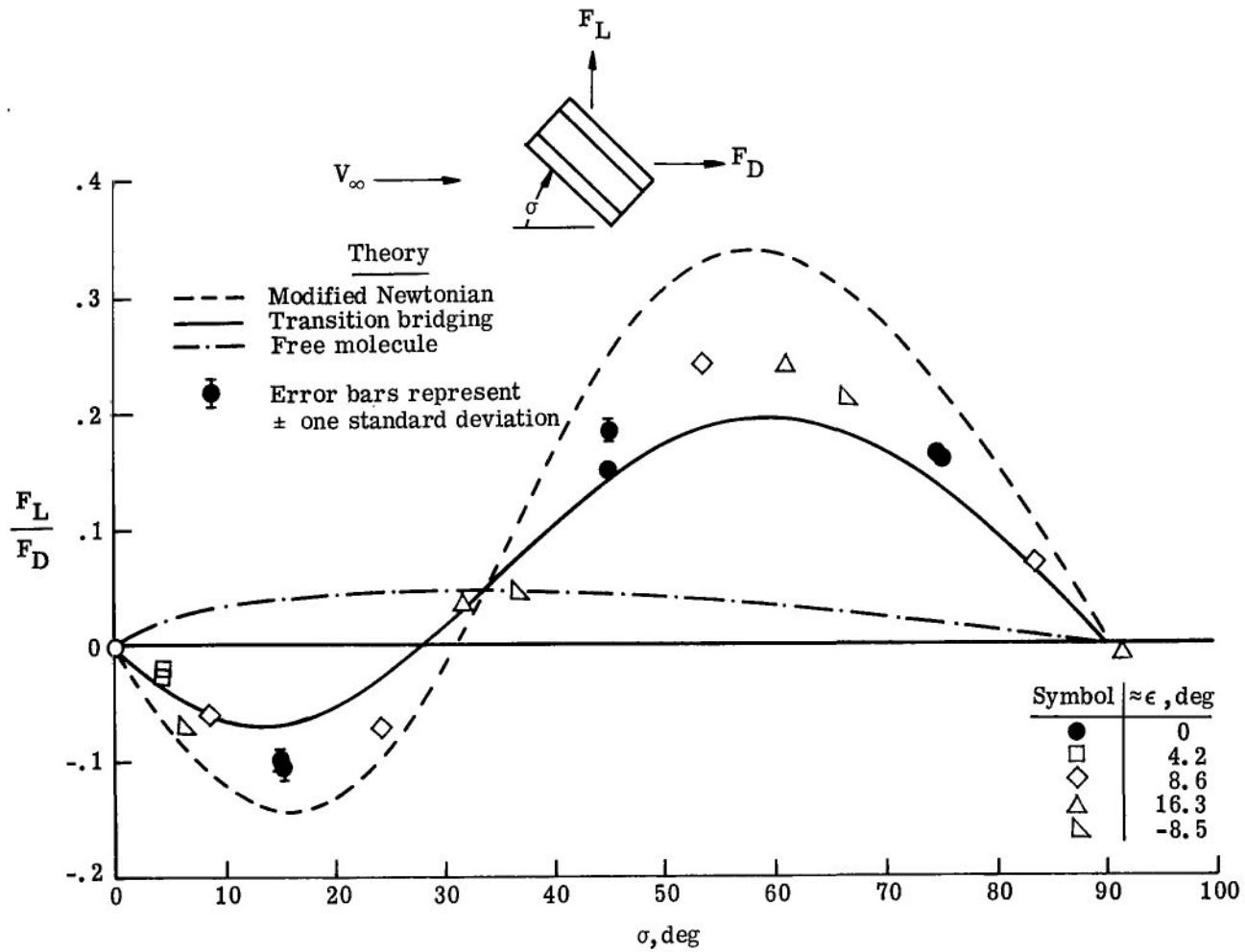
(c) Drag coefficient.

Figure 7.- Continued.



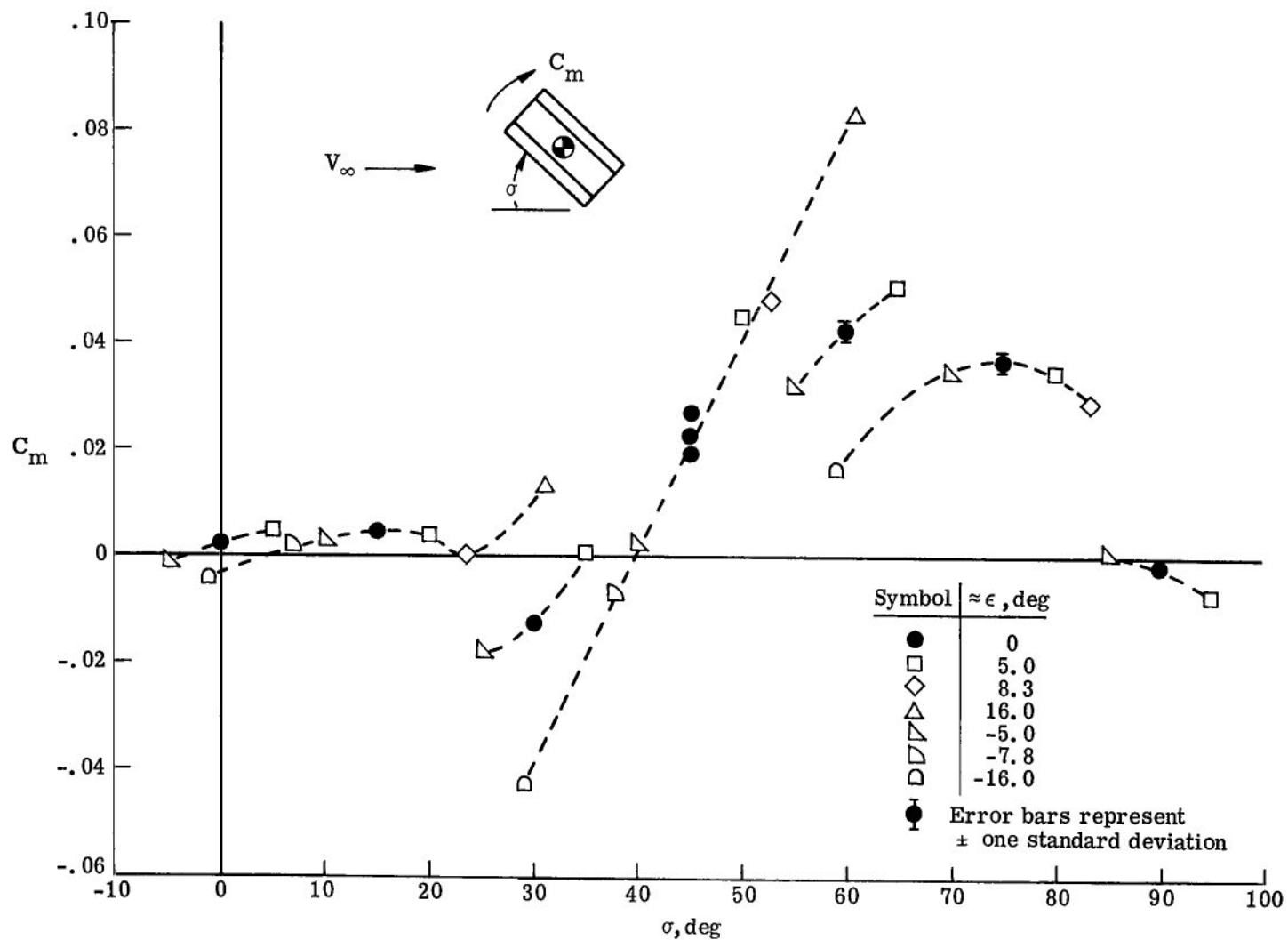
(d) Lift coefficient.

Figure 7.- Continued.



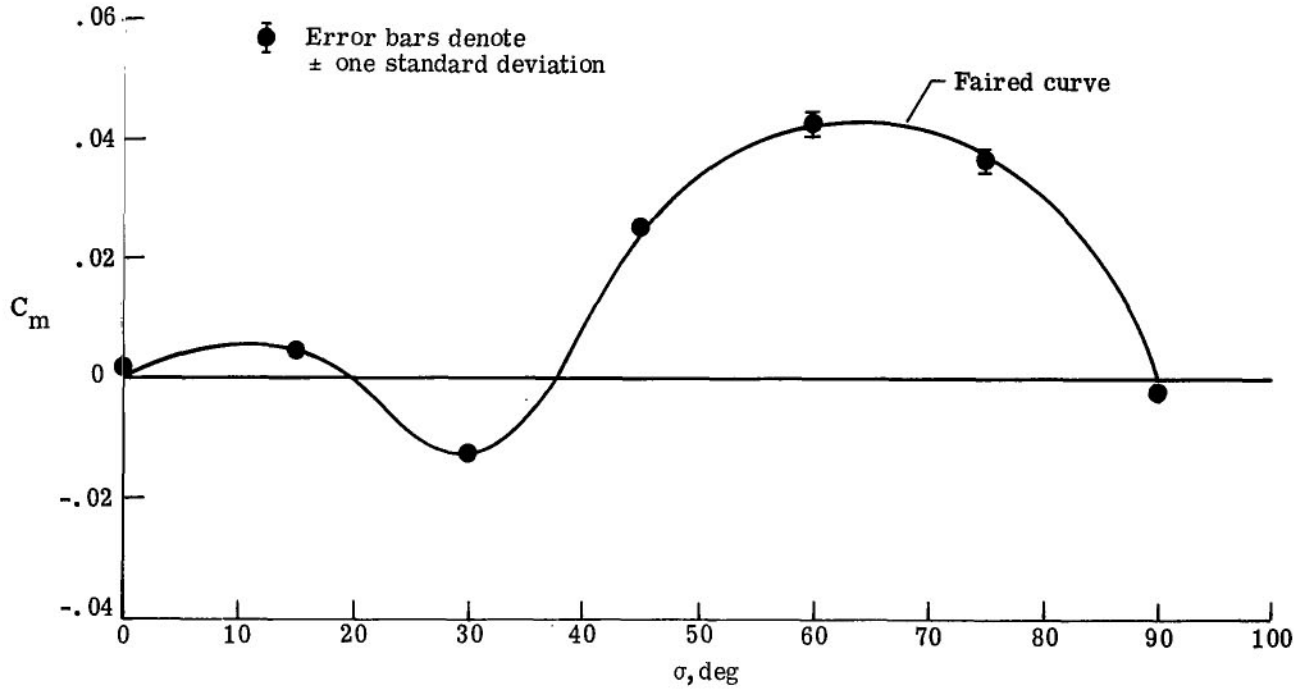
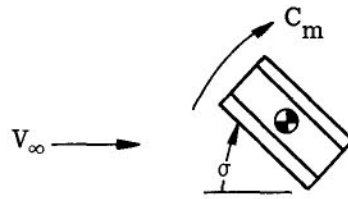
(e) Lift-drag ratio.

Figure 7.- Continued.



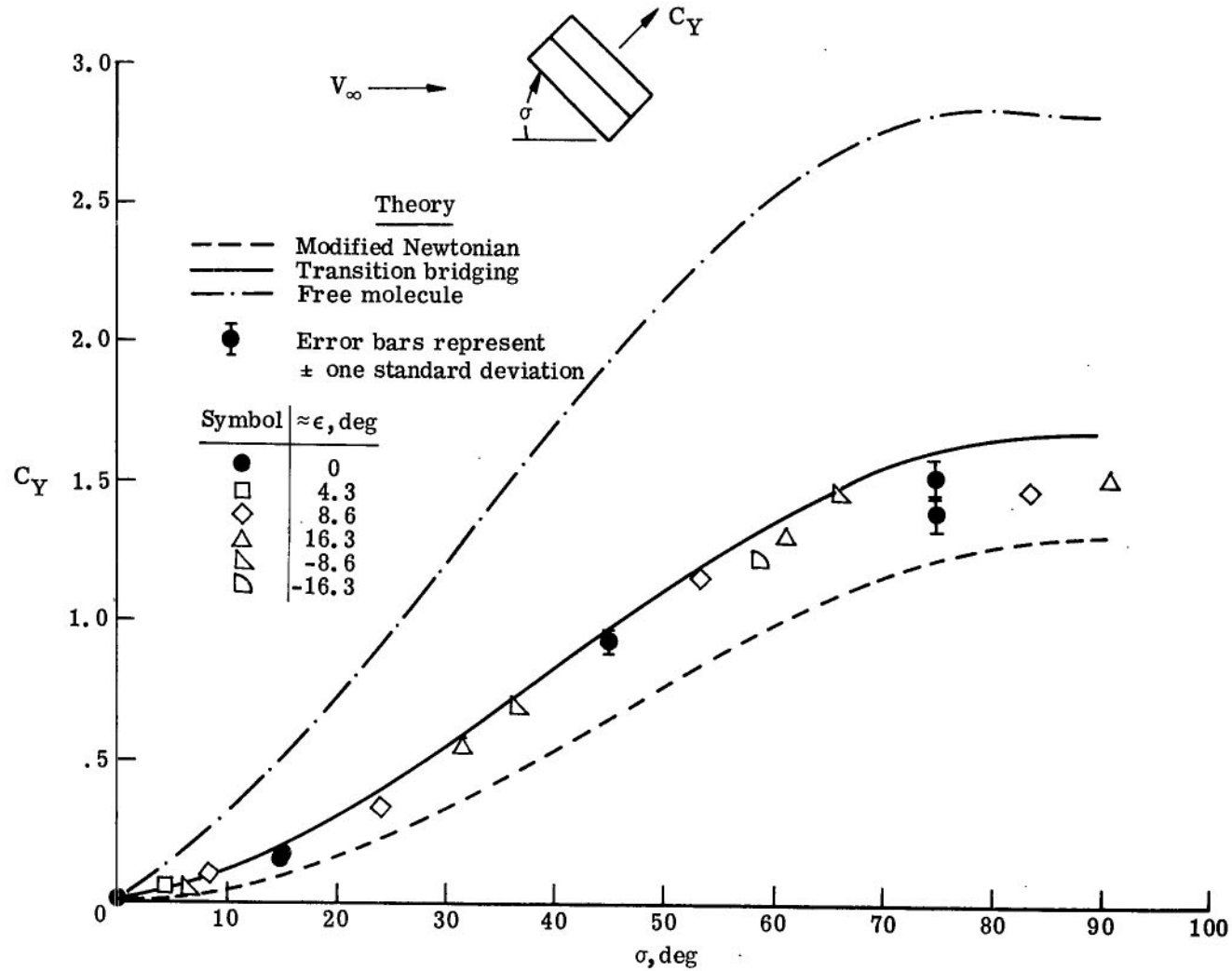
(f) Sting-interference effects on pitching-moment coefficient. Symbols connected by dashed lines are data taken with the same model.

Figure 7.- Continued.



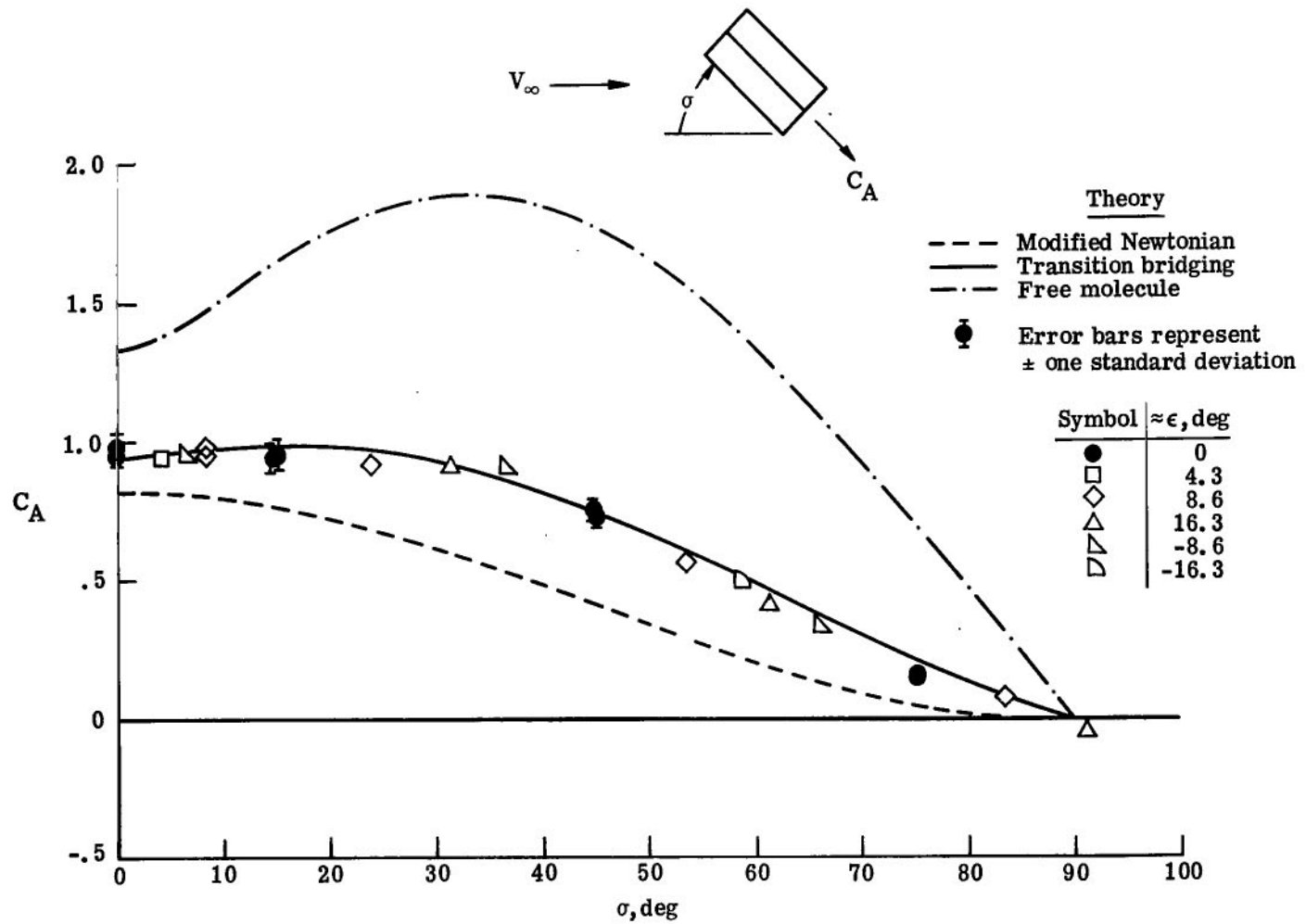
(g) Pitching-moment coefficient.

Figure 7.- Concluded.



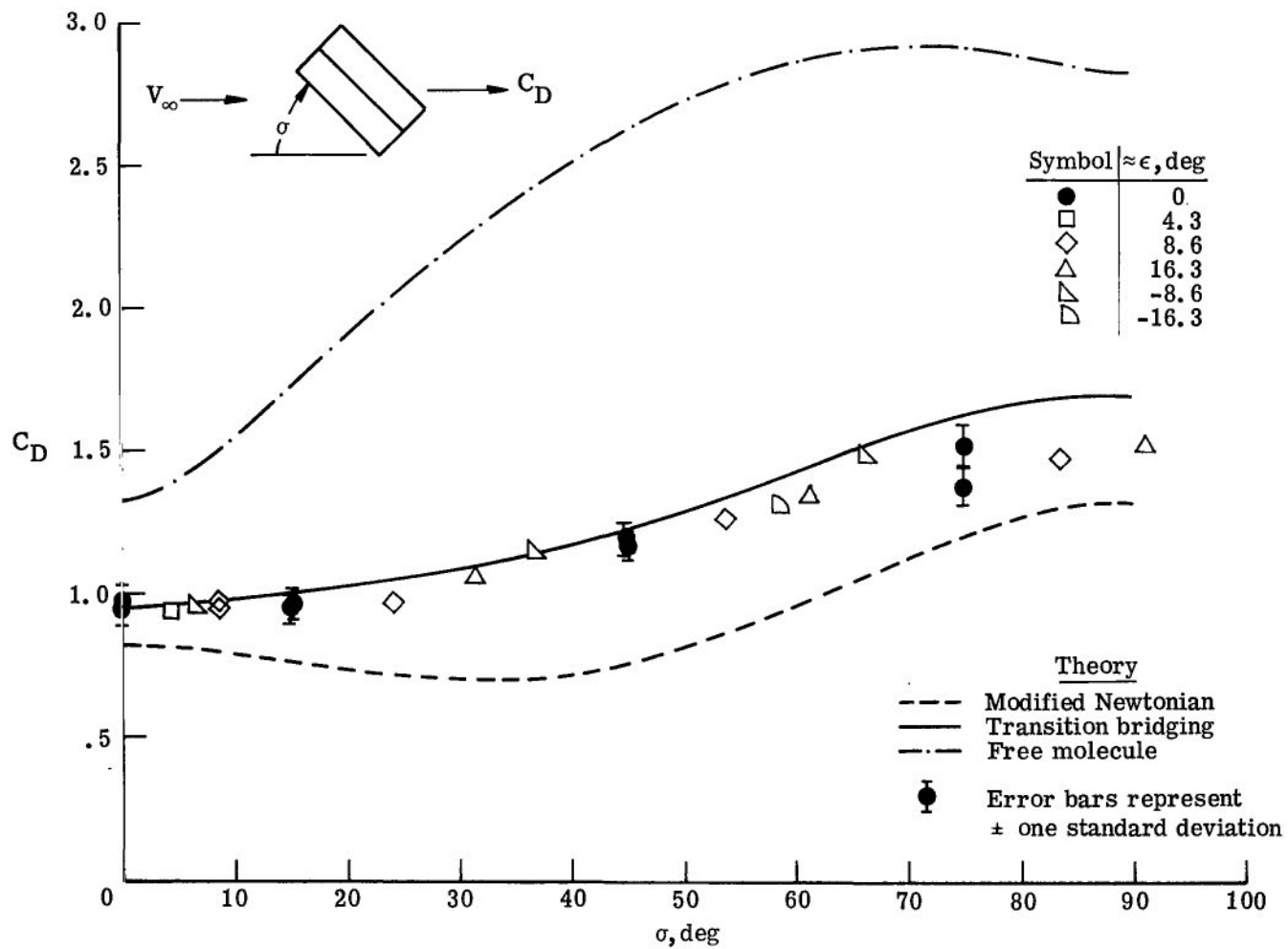
(a) Side-force coefficient.

Figure 8.- Lateral aerodynamic characteristics of a hexagonal prism.  $-\psi = 90^\circ$ .



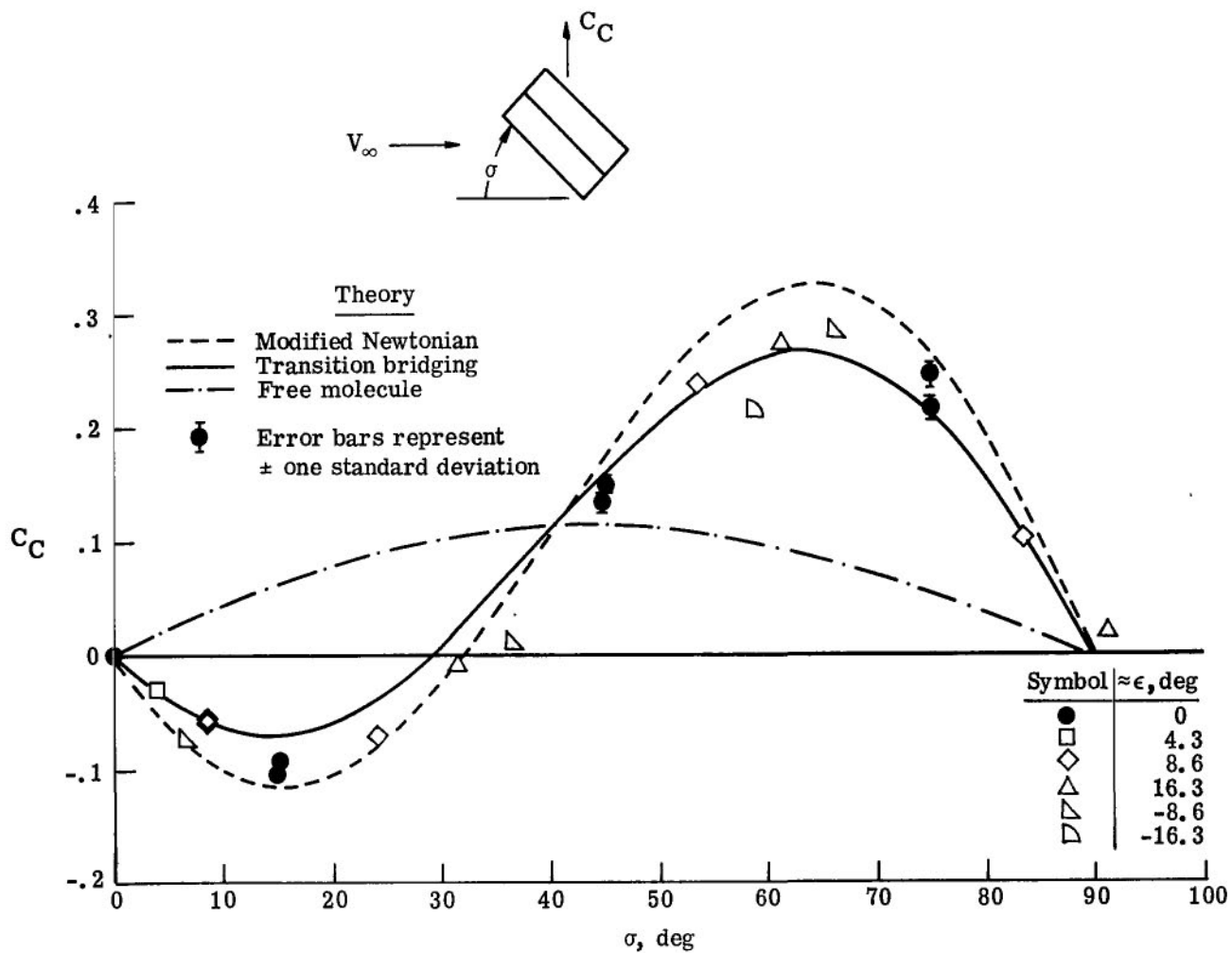
(b) Axial-force coefficient.

Figure 8.- Continued.



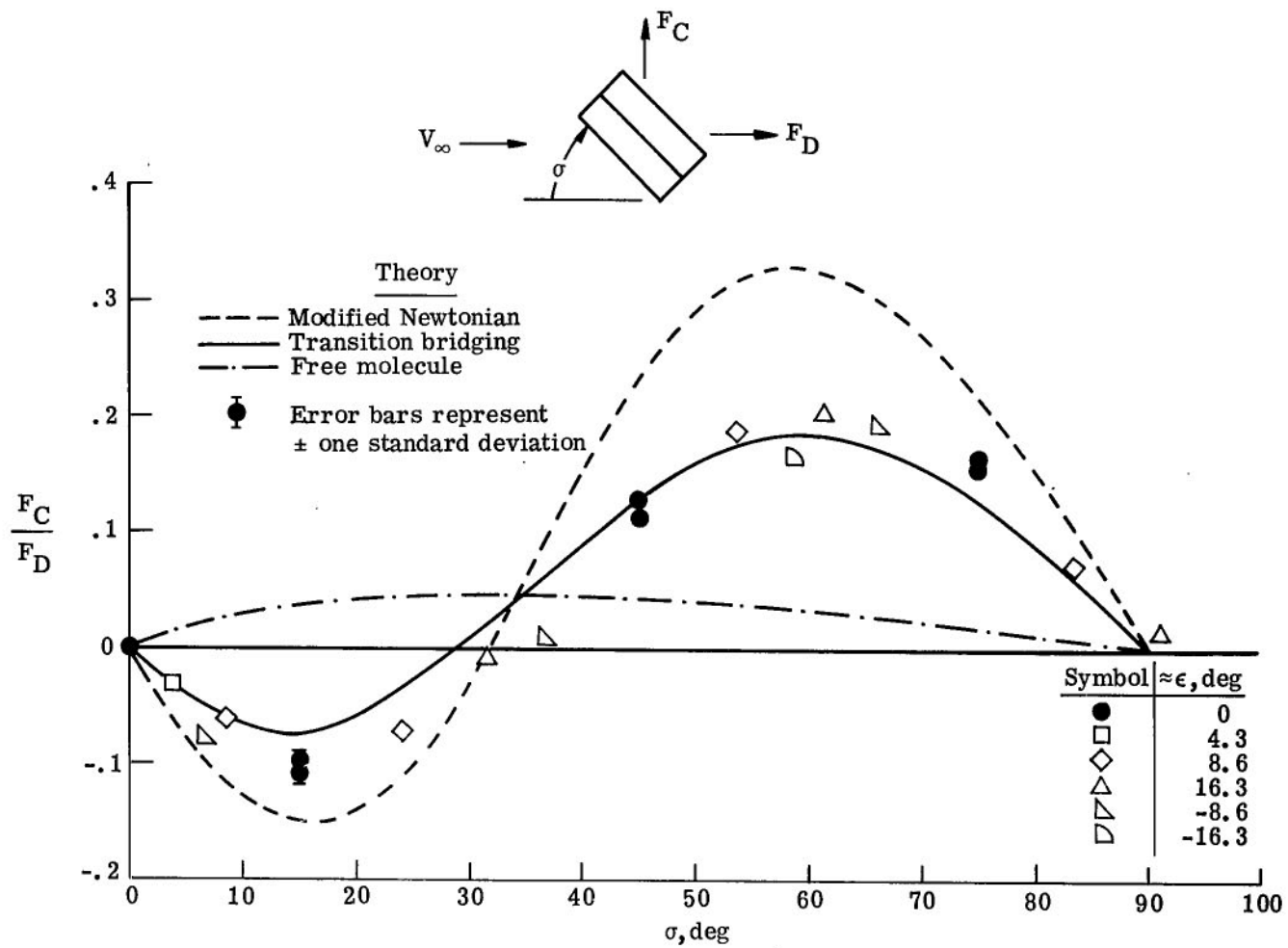
(c) Drag coefficient.

Figure 8.- Continued.



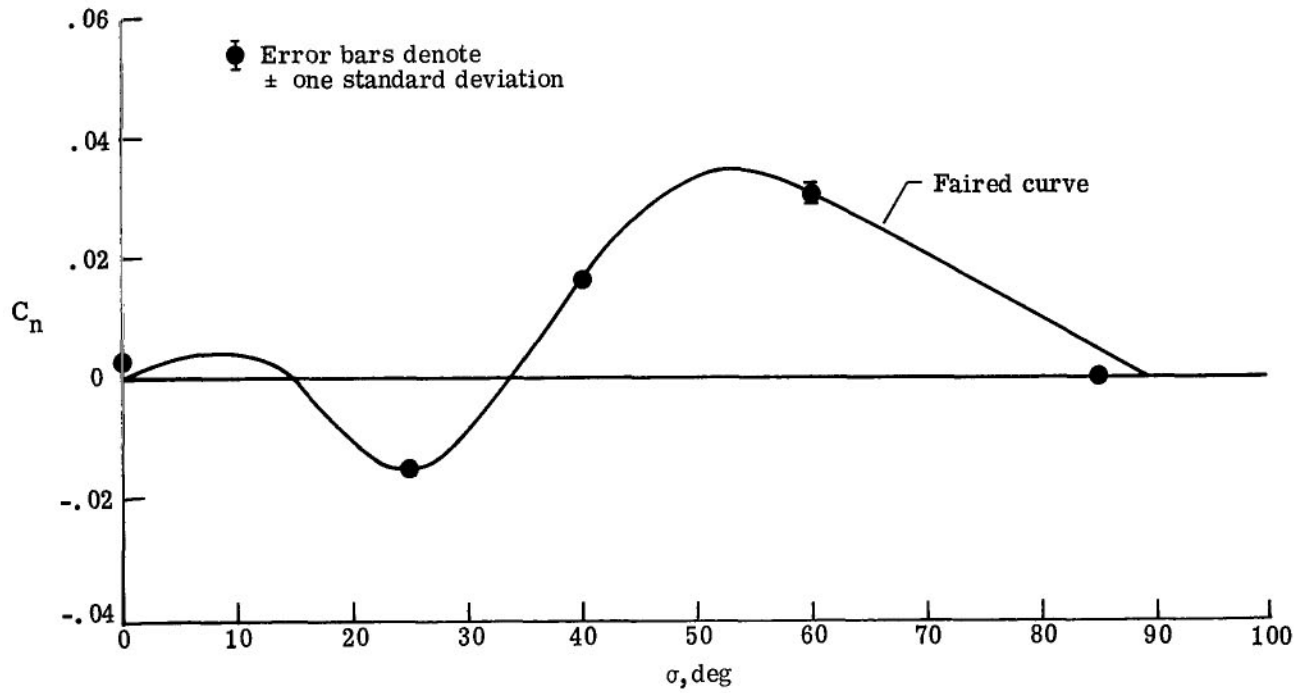
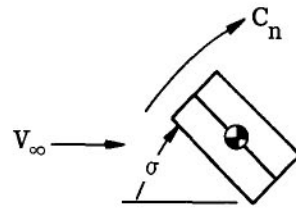
(d) Crosswind coefficient.

Figure 8.- Continued.



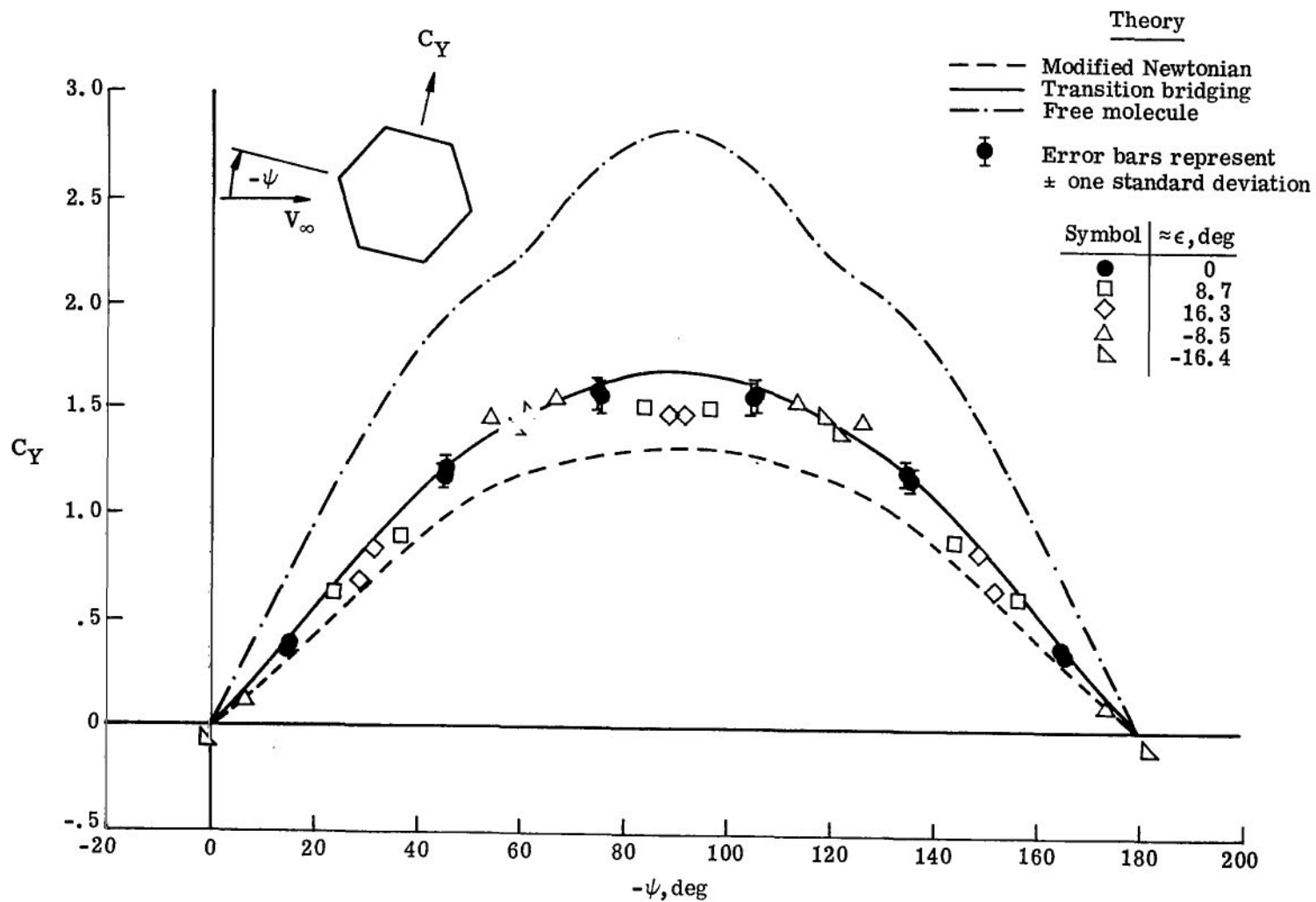
(e) Crosswind-drag ratio.

Figure 8.- Continued.



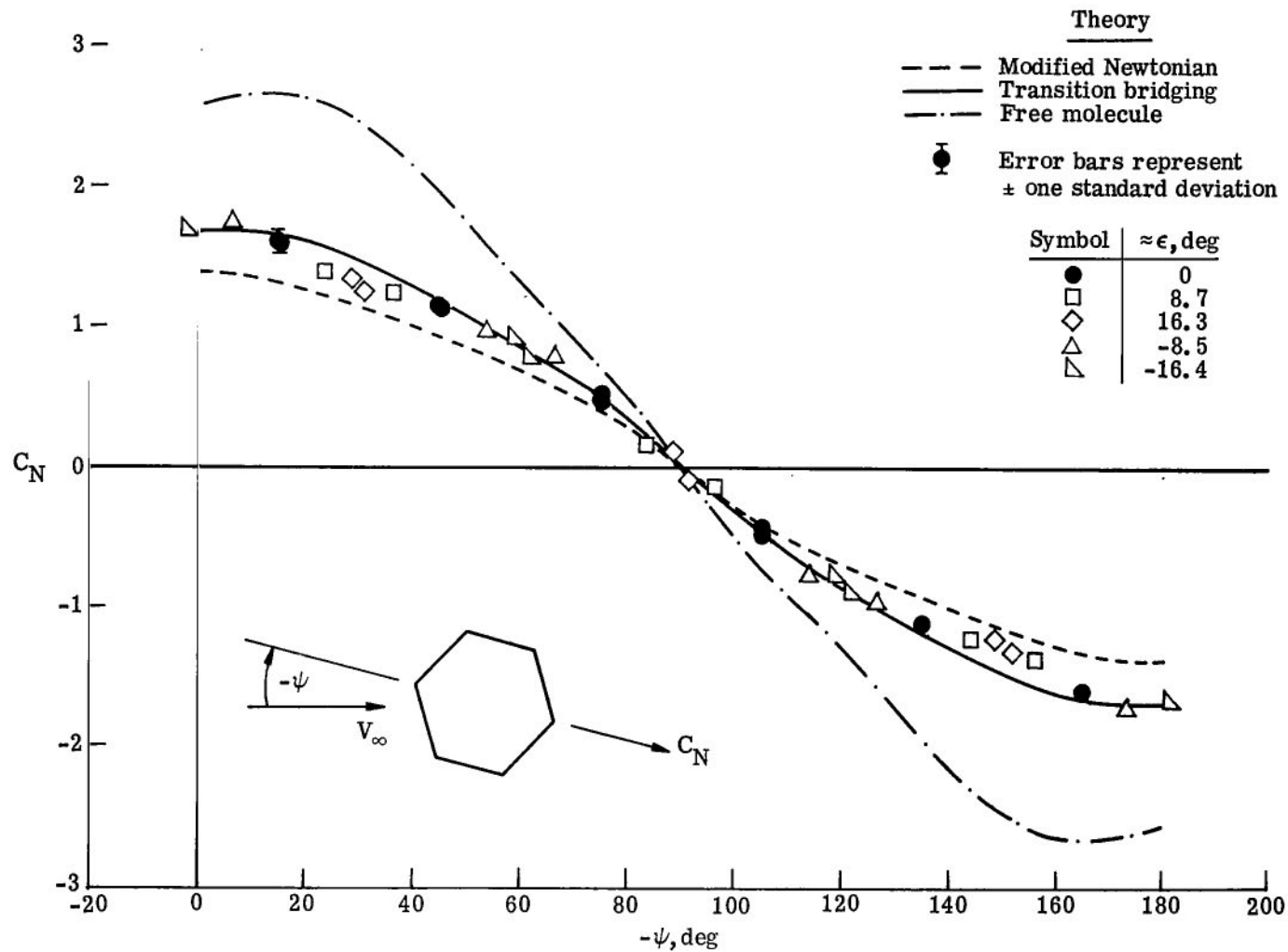
(f) Yawing-moment coefficient.

Figure 8.- Concluded.



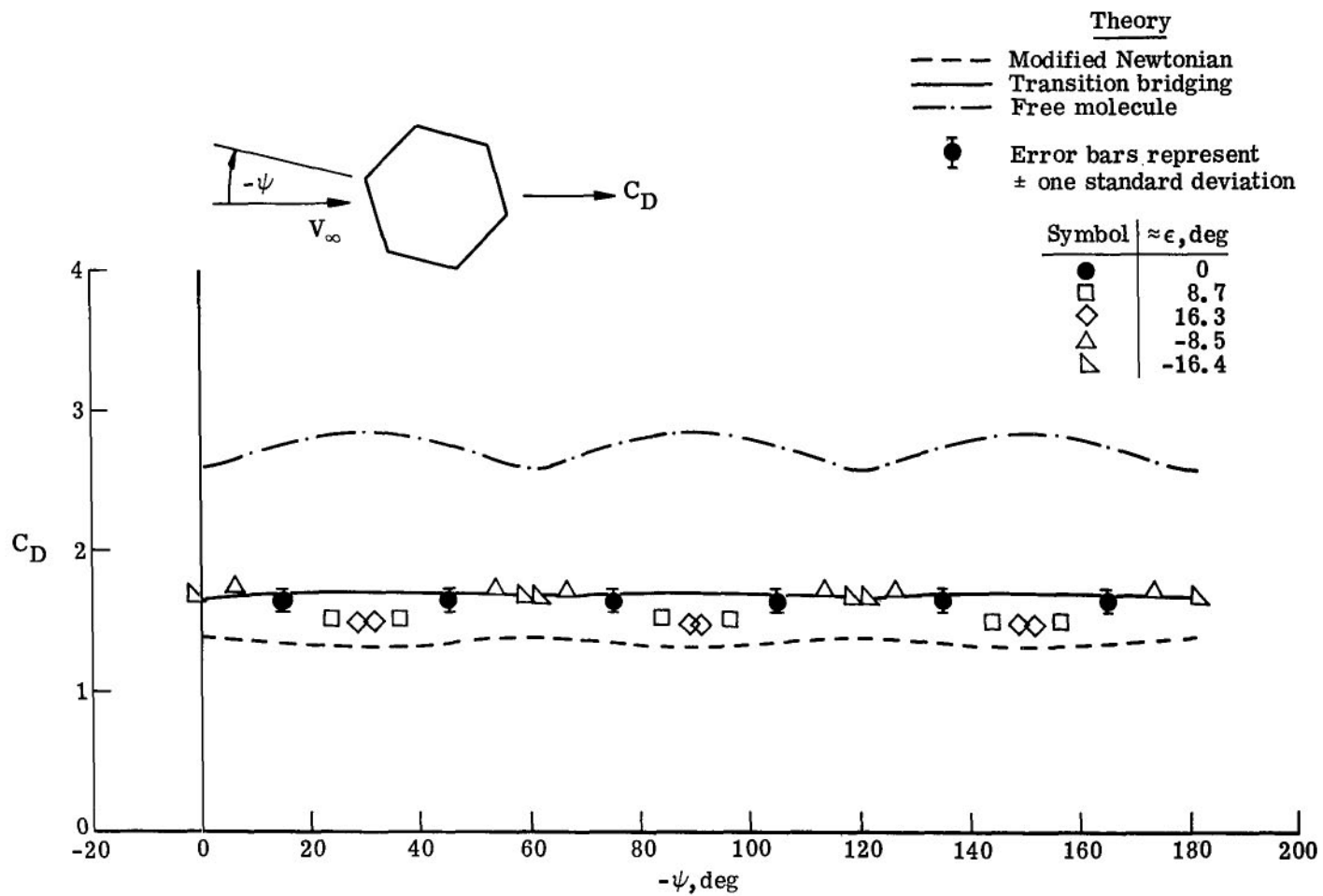
(a) Side-force coefficient.

Figure 9.- Roll characteristics of a hexagonal prism.  $\sigma = 90^\circ$ .



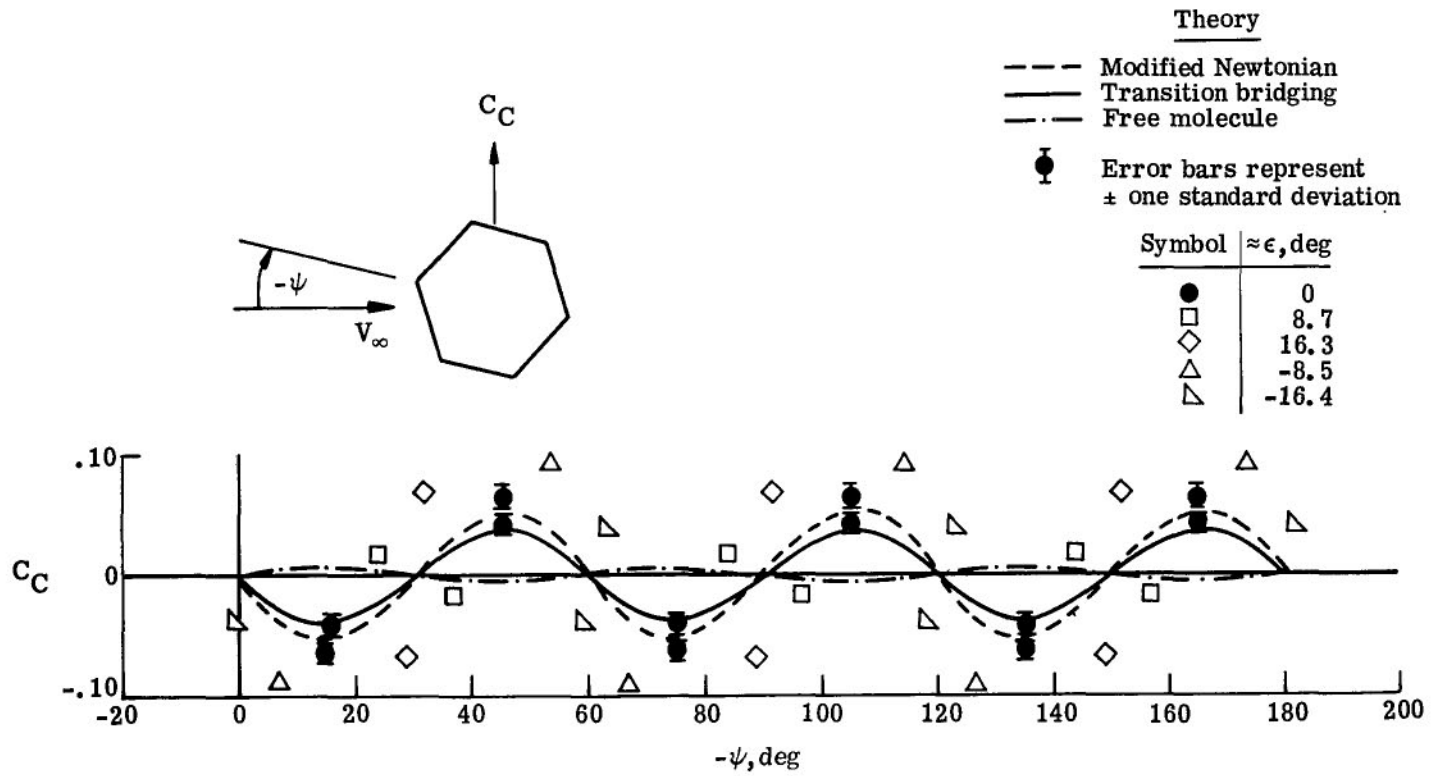
(b) Normal-force coefficient.

Figure 9.- Continued.



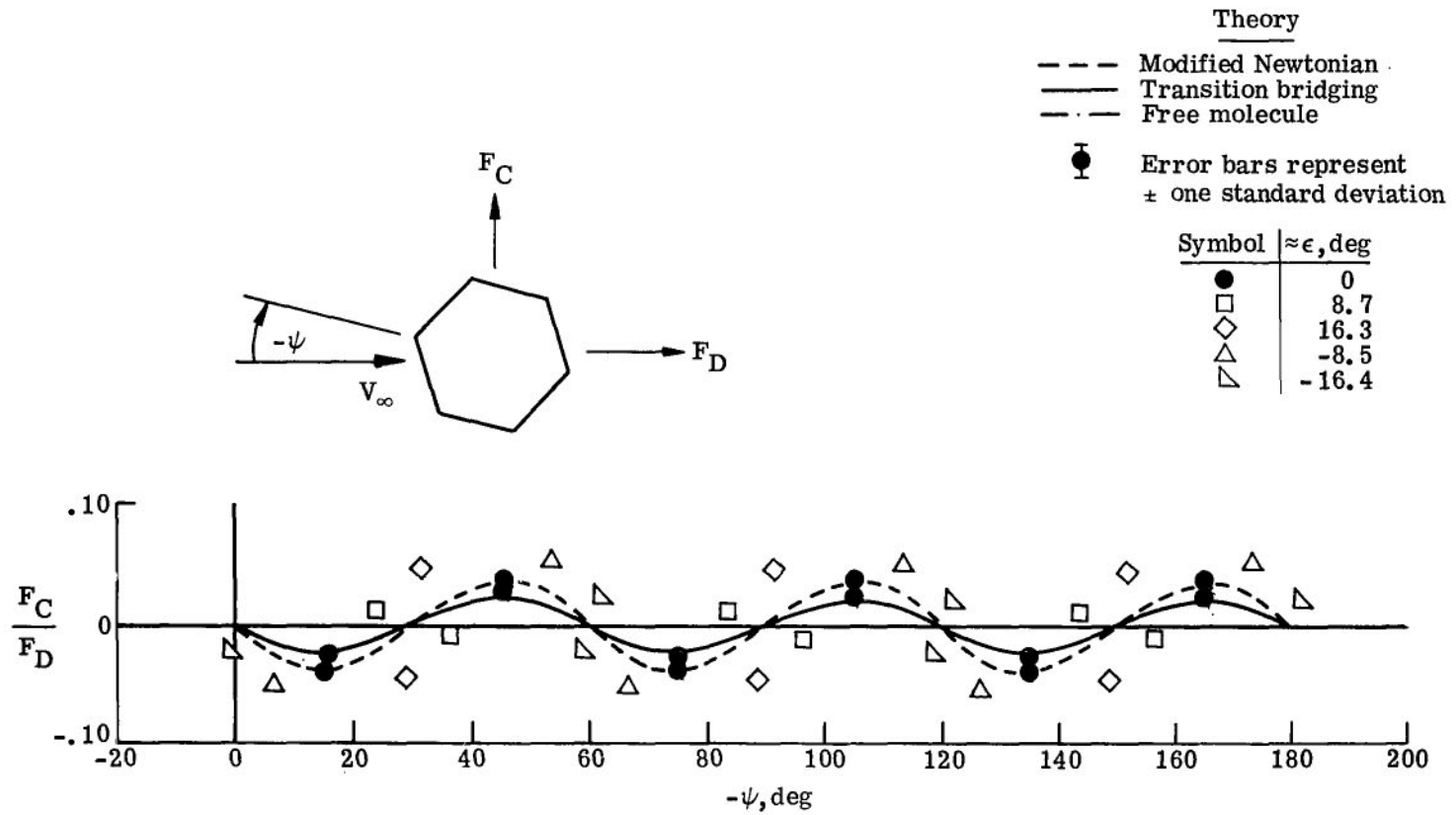
(c) Drag coefficient.

Figure 9.- Continued.



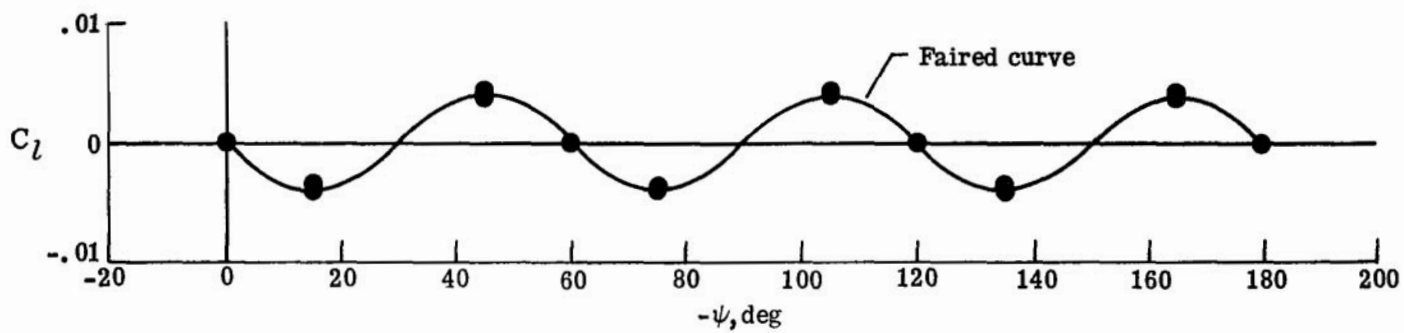
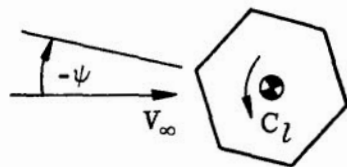
(d) Crosswind-force coefficient.

Figure 9.- Continued.



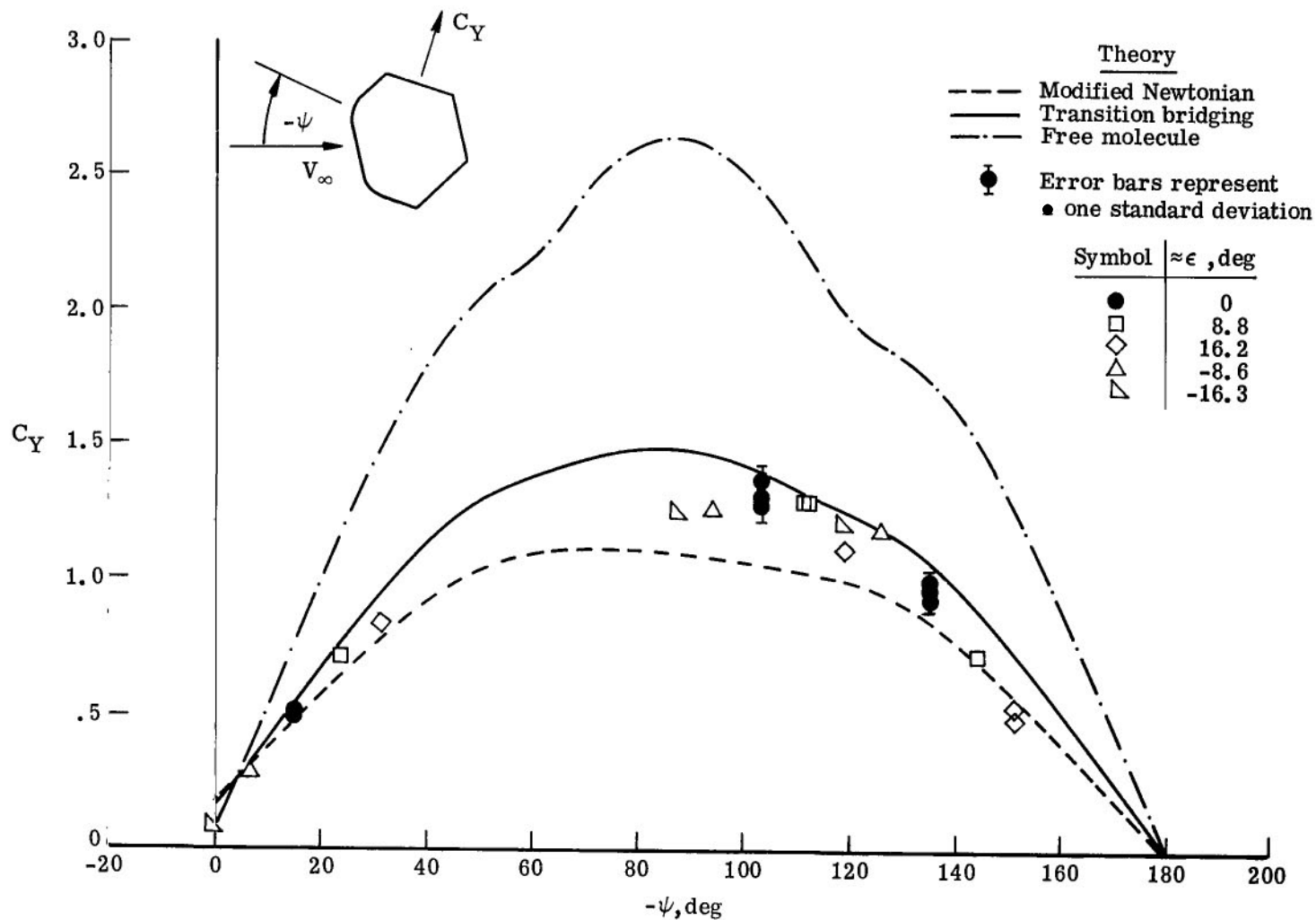
(e) Crosswind-drag ratio.

Figure 9.- Continued.



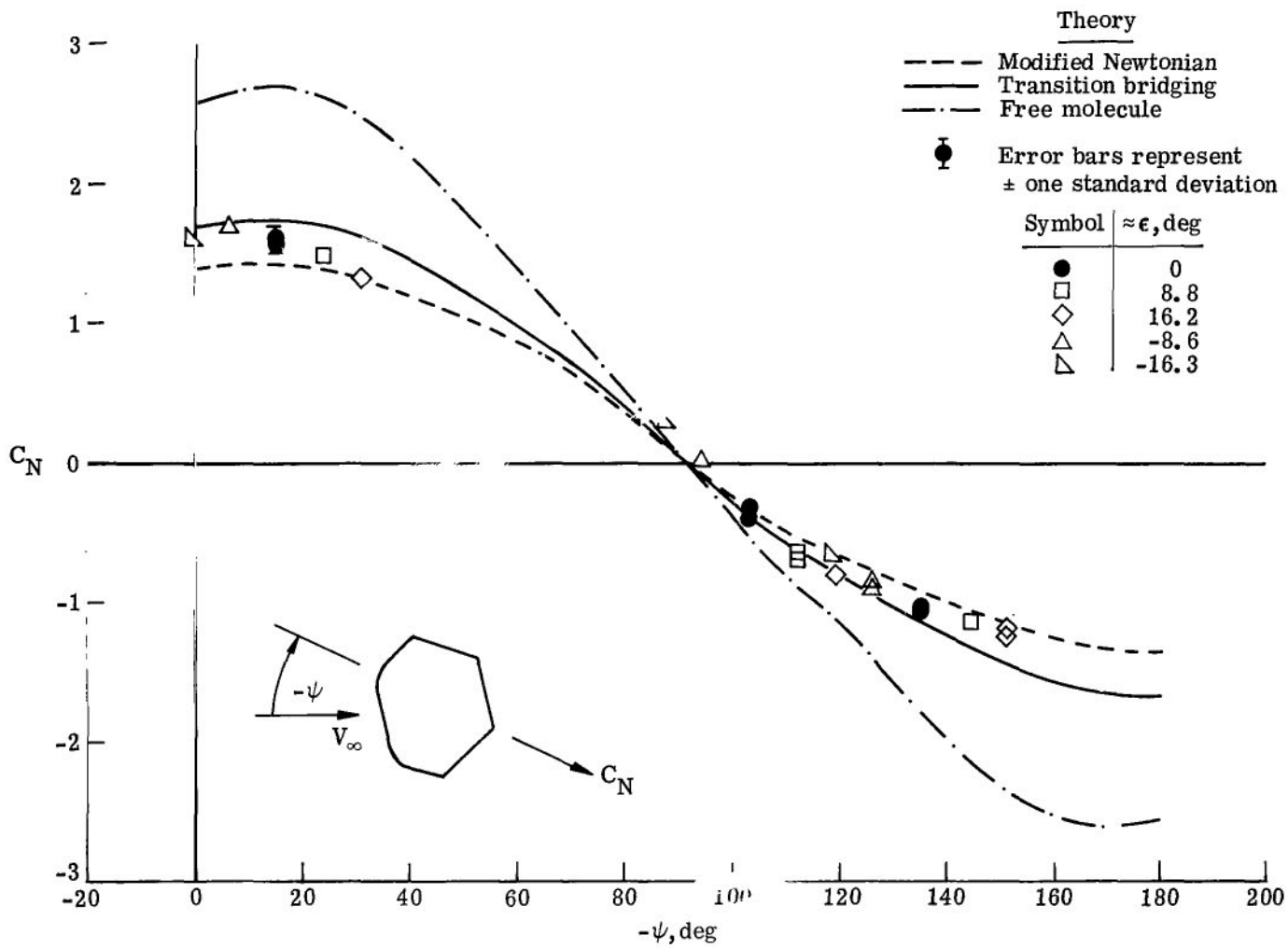
(f) Rolling-moment coefficient.

Figure 9.- Concluded.



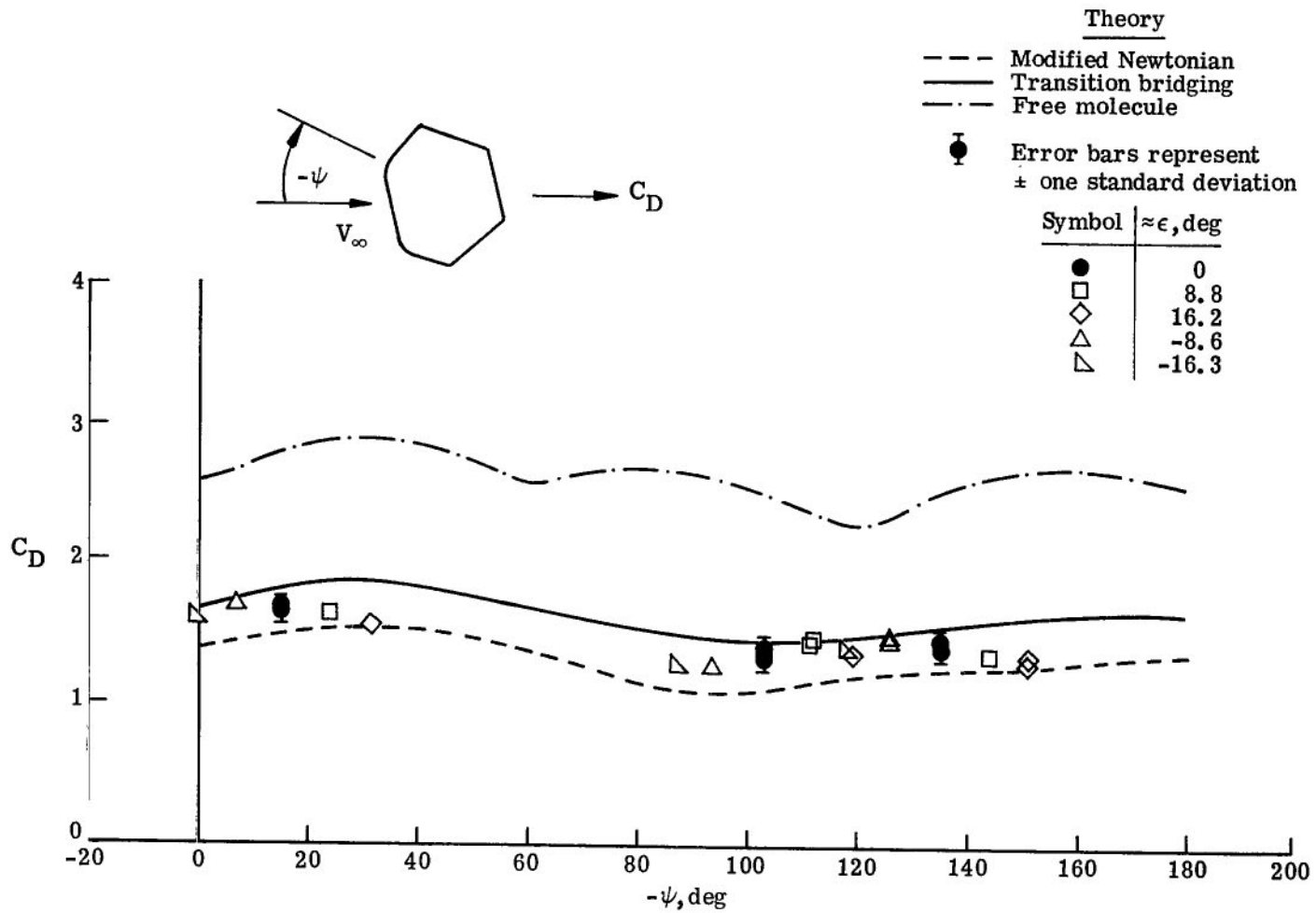
(a) Side-force coefficient.

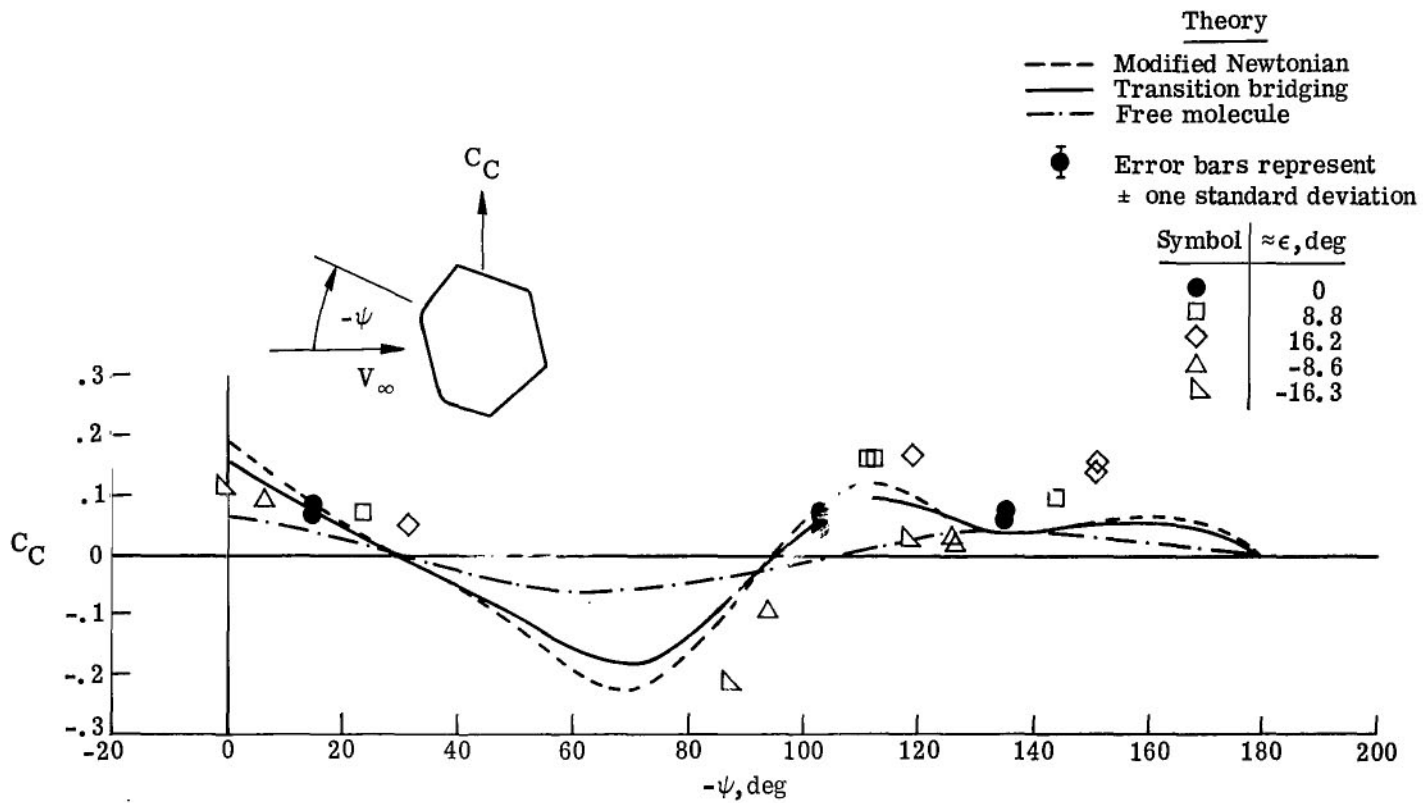
Figure 10.- Roll characteristics of a hexagonal prism with a simulated ablated flat.  $\sigma = 90^\circ$ .



(b) Normal-force coefficient.

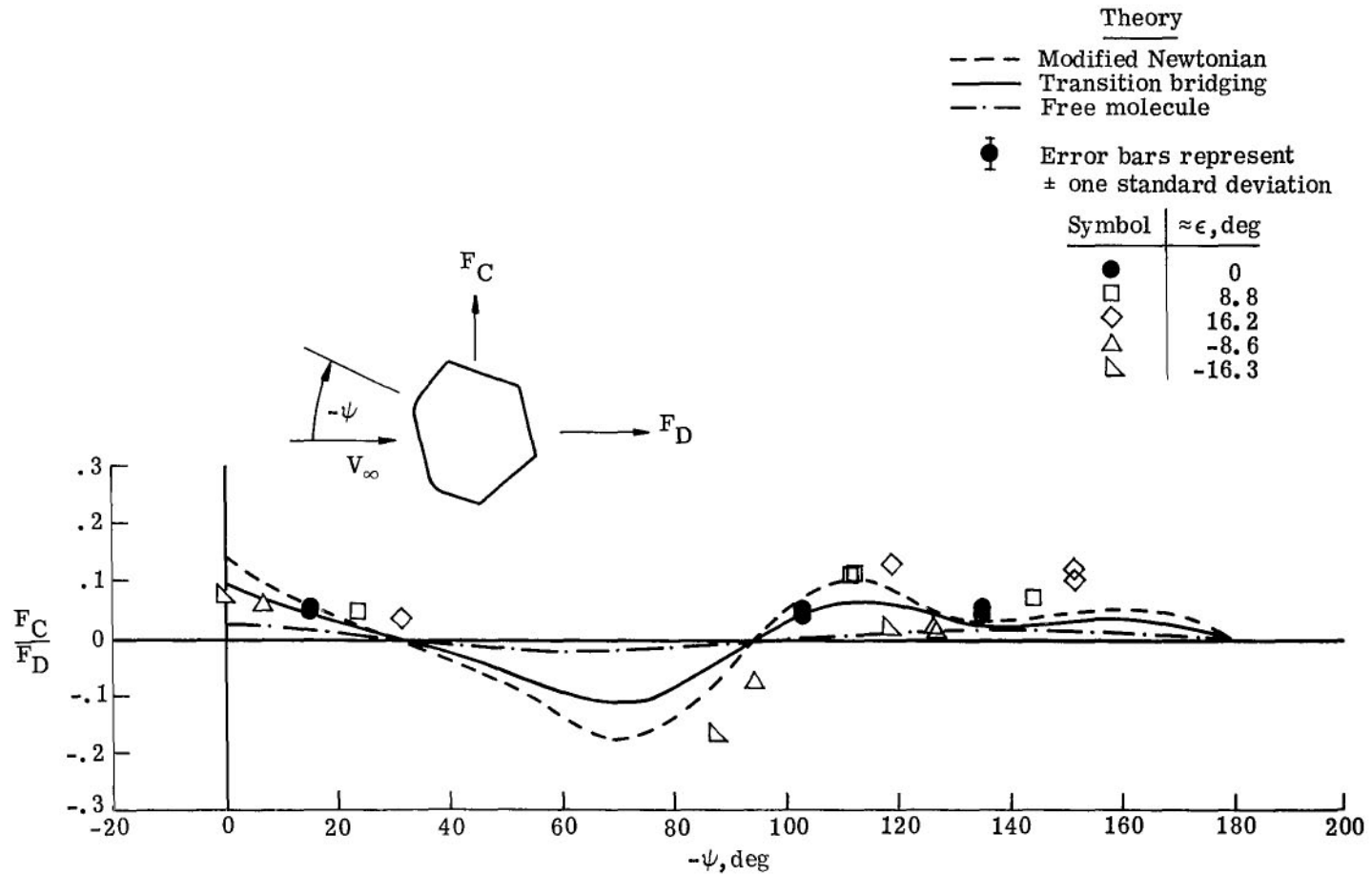
Figure 10.- Continued.





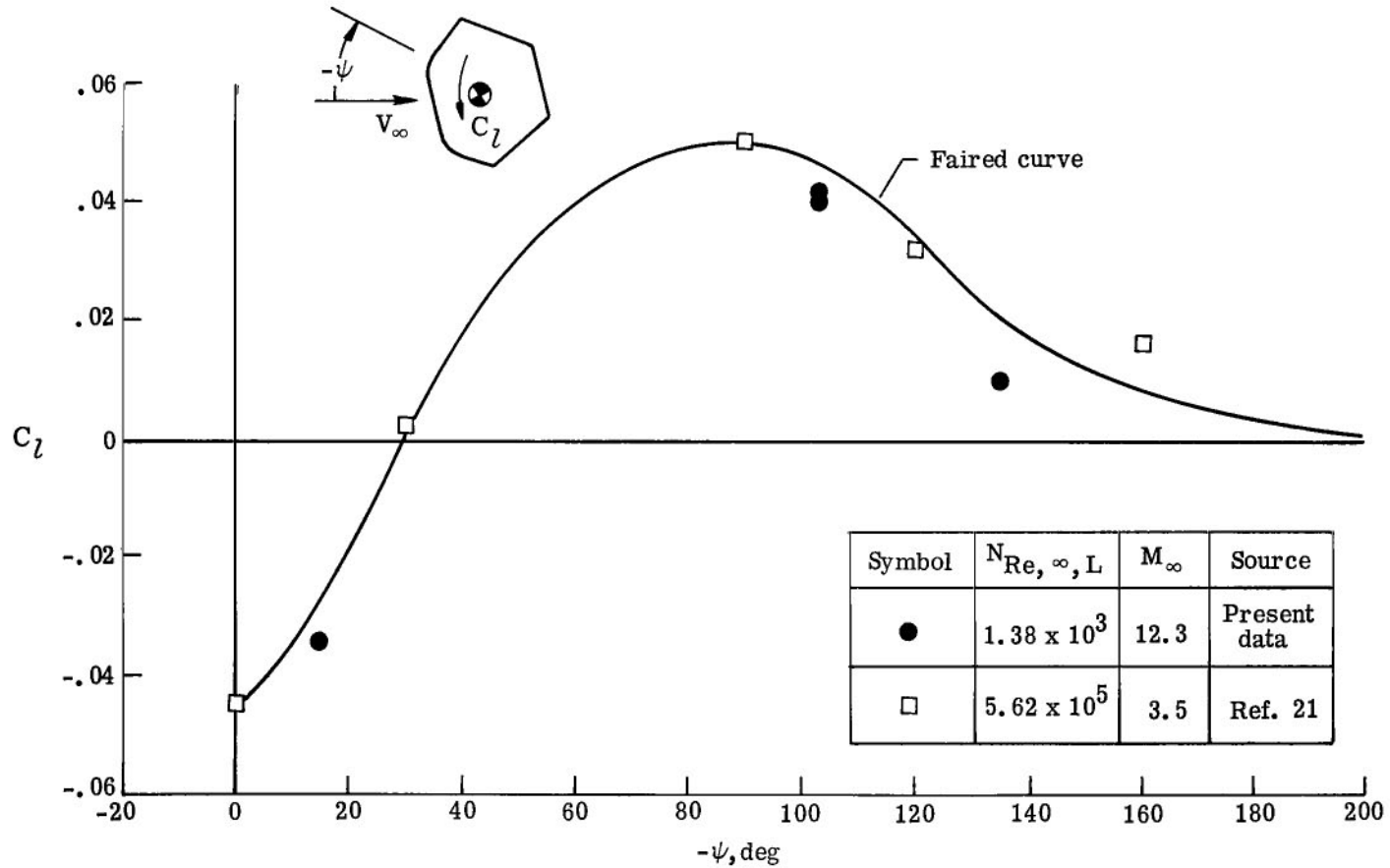
(d) Crosswind-force coefficient.

Figure 10.- Continued.



(e) Crosswind-drag ratio.

Figure 10.- Continued.



(f) Rolling-moment coefficient.

Figure 10.- Concluded.



017 001 C1 U 01 720609 S00903DS  
DEPT OF THE AIR FORCE  
AF WEAPONS LAB (AFSC)  
TECH LIBRARY/WLOL/  
ATTN: E LOU BOWMAN, CHIEF  
KIRTLAND AFB NM 87117

POSTMASTER: If Undeliverable (Section 15  
Postal Manual) Do Not Return

*"The aeronautical and space activities of the United States shall be conducted so as to contribute . . . to the expansion of human knowledge of phenomena in the atmosphere and space. The Administration shall provide for the widest practicable and appropriate dissemination of information concerning its activities and the results thereof."*

— NATIONAL AERONAUTICS AND SPACE ACT OF 1958

## NASA SCIENTIFIC AND TECHNICAL PUBLICATIONS

**TECHNICAL REPORTS:** Scientific and technical information considered important, complete, and a lasting contribution to existing knowledge.

**TECHNICAL NOTES:** Information less broad in scope but nevertheless of importance as a contribution to existing knowledge.

**TECHNICAL MEMORANDUMS:** Information receiving limited distribution because of preliminary data, security classification, or other reasons.

**CONTRACTOR REPORTS:** Scientific and technical information generated under a NASA contract or grant and considered an important contribution to existing knowledge.

**TECHNICAL TRANSLATIONS:** Information published in a foreign language considered to merit NASA distribution in English.

**SPECIAL PUBLICATIONS:** Information derived from or of value to NASA activities. Publications include conference proceedings, monographs, data compilations, handbooks, sourcebooks, and special bibliographies.

**TECHNOLOGY UTILIZATION PUBLICATIONS:** Information on technology used by NASA that may be of particular interest in commercial and other non-aerospace applications. Publications include Tech Briefs, Technology Utilization Reports and Technology Surveys.

*Details on the availability of these publications may be obtained from:*

**SCIENTIFIC AND TECHNICAL INFORMATION OFFICE  
NATIONAL AERONAUTICS AND SPACE ADMINISTRATION  
Washington, D.C. 20546**